IOP Publishing Plasma Sources Science and Technology

Plasma Sources Sci. Technol. **23** (2014) 035014 (18pp) doi:10.1088/0963-0252/23/3/035014

Particle-in-cell and global simulations of α to γ transition in atmospheric pressure Penning-dominated capacitive discharges

E Kawamura[1], M A Lieberman[1], A J Lichtenberg[1], P Chabert[2] and C Lazzaroni[3]

[1] Department of Electrical Engineering and Computer Sciences, University of California, Berkeley, CA 94720, USA
[2] LPP, CNRS, Ecole Polytechnique, UPMC, Paris XI, 91128 Palaiseau, France
[3] LSPM, CNRS, Universite Paris 13, Sorbonne Paris Cite, 93430 Villetaneuse, France

Received 14 January 2014, revised 19 March 2014
Accepted for publication 16 April 2014
Published 19 May 2014

Abstract

Atmospheric pressure radio-frequency (rf) capacitive micro-discharges are of interest due to emerging applications, especially in the bio-medical field. A previous global model did not consider high-power phenomena such as sheath multiplication, thus limiting its applicability to the lower power range. To overcome this, we use one-dimensional particle-in-cell (PIC) simulations of atmospheric He/0.1%N_2 capacitive discharges over a wide range of currents and frequencies to guide the development of a more general global model which is also valid at higher powers. The new model includes sheath multiplication and two classes of electrons: the higher temperature 'hot' electrons associated with the sheaths, and the cooler 'warm' electrons associated with the bulk. The electric field and the electron power balance are solved analytically to determine the time-varying hot and warm temperatures and the effective rate coefficients. The particle balance equations are integrated numerically to determine the species densities. The model and PIC results are compared, showing reasonable agreement over the range of currents and frequencies studied. They indicate a transition from an α mode at low power characterized by relatively high electron temperature T_e with a near uniform profile to a γ mode at high power with a T_e profile strongly depressed in the bulk plasma. The transition is accompanied by an increase in density and a decrease in sheath widths. The current and frequency scalings of the model are confirmed by the PIC simulations.

Keywords: atmospheric pressure plasma discharges, alpha to gamma transition, particle-in-cell simulations

(Some figures may appear in colour only in the online journal)

1. Introduction

Atmospheric pressure radio-frequency (rf) micro-discharges have been extensively studied due to emerging applications in the bio-medical and materials processing fields. Although not hard to implement experimentally [1–5], diagnostics are difficult due to their small size, leading to a need for efficient and accurate numerical modeling. Since many species and reactions are involved, global models with averages over space and time are useful for their computational efficiency [6–8]. Alternatively, spatial variation can be considered in one-dimensional (1D) fluid or fully kinetic particle-in-cell (PIC) simulations [9–16], but the increased complexity leads to increased computation times and limits the parameter range. Recently, a review of atmospheric pressure plasma modeling and experiments has appeared with extensive references [17].

In a previous work [18], a fast hybrid analytical–numerical global model was developed to simulate atmospheric pressure rf discharges. In the model, the ion density n_i is assumed to be uniform over the gap width l while the electron density n_e is uniform with $n_e = n_i$ over a cloud of width $d = l - s_m$, where s_m is the maximum value of the oscillating sheath width. An

analytical solution of a current-driven homogeneous discharge yields the space- and time-varying electric field $E(x,t)$ and the oscillating sheath width $s(t)$. An ohmic power balance is then used to find the time-varying electron temperature $T_e(t)$ on the rf timescale. An analytical average over an rf period yields the effective electron rate coefficients used in the particle balance equations, which are numerically integrated to find the global species densities. The model results were compared with 1D fluid calculations [14, 15] for atmospheric He/0.1%N_2 and He/0.5%O_2 discharges with discharge gap $l = 1$ mm and rf driving frequency $f = 13.56$ MHz over a relatively low power range $S_{abs} = 3$–33 kW m^{-2}. The neutral and charged particle densities and reaction rates mainly agreed within a factor of two, becoming less accurate at the higher powers.

At high powers, the sheath electric fields can be large enough to produce avalanche multiplication of electrons created either by ion-impact secondary emission from the electrodes, or by metastable electron–ion pair production within the sheaths. These processes produce a higher temperature 'hot' electron group which is neglected in the global model [18], thus limiting its application to the lower power regime. Other model inaccuracies can arise from neglecting spatial variations. For example, the high fields in the sheath regions lead to higher metastable densities in the sheaths.

In this paper, we perform 1D PIC simulations of a capacitive atmospheric pressure He discharge with trace amounts of N_2, over a wide range of input currents and frequencies. Both time-averaged as well as space- and time-varying PIC diagnostics are available to provide a detailed description of the physics. We use the results to guide the development of an improved global model applicable to the higher power regimes. The improved model includes sheath multiplication and two classes of electrons: the higher temperature hot electrons associated with the sheaths, and the cooler warm electrons associated with the bulk. In addition, a separate Child law (CL) sheath calculation is performed to determine the ion wall loss flux Γ_w.

In section 2.1, the PIC method is described, and the choice of species and reactions is discussed. In section 2.2, we present and discuss PIC simulation results of a 1 mm gap atmospheric He/0.1%N_2 discharge for the base case of applied frequency $f = 27.12$ MHz. PIC results at $f = 13.56$ MHz are also presented and compared with the base case. In section 3, we present the improved global model. In section 4, the global and PIC results are compared for a wide range of input rf current densities and frequencies. The results are explained in terms of the analytical scaling, and differences are discussed. In section 5, we present the conclusions.

2. PIC simulations

2.1. PIC code description

Kinetic PIC simulations obtain the fields, particle densities and fluxes self-consistently from first principles, without making any assumptions about the particle temperatures or velocity distributions. The simulations were conducted using the planar bounded plasma electrostatic 1D3v code XPDP1 [19, 20]. In the code, each computer particle represents a cluster of 10^6 to 10^8 real particles (e.g. electrons, ions or metastables). For each computer particle, XPDP1 tracks the (1D) displacement in the axial (x) direction and the velocity components in all three directions (3v). The simulation is run with a sufficient number of particles to minimize the discrete particle noise; i.e. $N_c, N_D \gg 1$, where N_c and N_D are the number of particles per cell and the number of particles per Debye length (λ_D), respectively. The neutrals in XPDP1 are assumed to form a constant and uniform background gas with a fixed temperature. Collisions between the particles and the background gas are included in the simulations using a Monte-Carlo collision (MCC) algorithm. A description of the null collision method used in our code is given in [20].

In a typical electrostatic PIC simulation, for each timestep Δt, (i) particles are linearly weighted to the spatial grid to obtain the charge density ρ_j at the grid points, (ii) ρ_j is used in Poisson's equation to solve for the electric field E_j at the grid points, (iii) E_j is linearly interpolated to each particle position x_i to determine the force F_i on each particle, (iv) the Newton–Lorenz equation of motion is used to advance the particles to new positions and velocities via an explicit leap frog integration scheme, (v) boundaries are checked and out of bound particles are removed while injected particles such as secondary electrons are introduced, (vi) a MCC handler, using the null collision method, checks for collisions and adjusts the particle velocities and numbers accordingly.

To ensure the stability and accuracy for the leap frog method, the timestep Δt must resolve the electron plasma frequency $\omega_p \equiv (e^2 n_e/\epsilon_0 m_e)^{1/2}$ while the grid spacing Δx should be of the same order as the electron Debye length $\lambda_D \equiv (\epsilon_0 T_e/e n_e)^{1/2}$. To ensure the accuracy of the null collision method, Δt must be small enough that the probability of more than one collision per particle per Δt is low; i.e. $\nu_{max}\Delta t \ll 1$, where ν_{max} is the maximum collision frequency of the simulated discharge. This last constraint is typically the most important when determining Δt for high-pressure atmospheric discharges.

For efficient PIC simulations, we used a simplified model of an He gas discharge with trace amounts of N_2 with only three species: electrons, N_2^+ and He*. A previous global model [18] of an He/0.1%N_2 discharge included six species: electrons, N_2^+, He*, He_2^*, He^+ and He_2^+. However, this model showed that for atmospheric He/0.1%N_2 discharges, the He^+ and He_2^+ densities were about three orders of magnitudes below the N_2^+ density, and the He_2^* density was much smaller (by about a factor of 3) than the He* density (see figure 6 in [18]). Thus, we considered interactions involving He^+ and He_2^+, He_2^* to be unimportant in capturing the basic He/0.1%N_2 discharge dynamics, and devised a simplified three species cross-section set consisting of electrons, N_2^+ ions and He* metastables. This enabled us to considerably speed up the PIC code by tracking only these three species.

The He/N_2 reaction rate coefficient set in [18] is used to develop the simplified PIC cross-section set.

(1) e + He → e + He, elastic scattering
(2) e + N_2 → e + e + N_2^+, Ionization

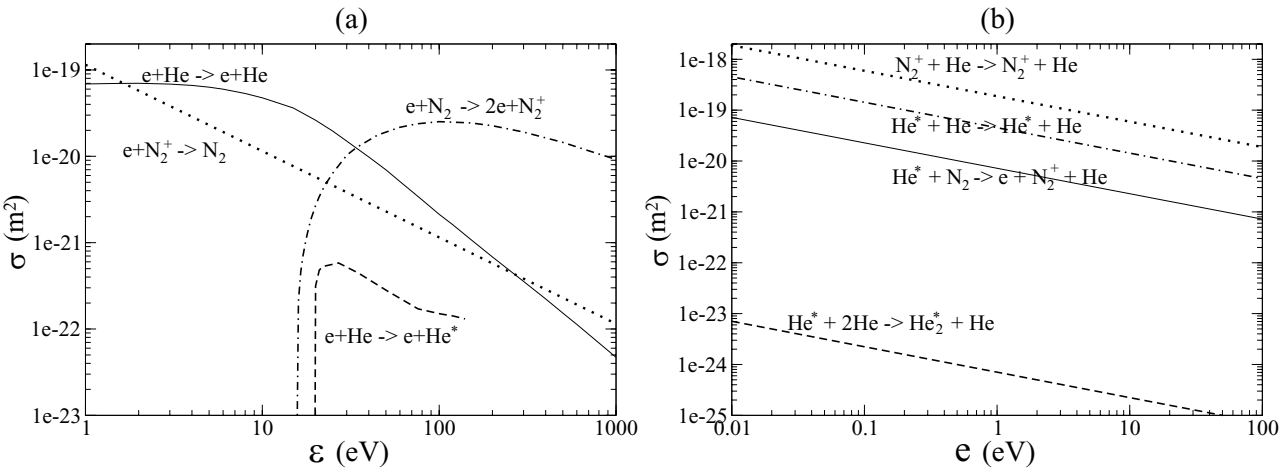

Figure 1. PIC cross-sections (m^2) versus incident particle energy $\mathcal{E}$ (eV) for (*a*) electron–neutral and electron–ion recombination collisions and (*b*) ion–neutral and metastable–neutral collisions.

(3) $e + N_2^+ \rightarrow N + N$, recombination (N is not followed in the PIC)
(4) $N_2^+ + He \rightarrow N_2^+ + He$, ion elastic scattering
(5) $e + He \rightarrow e + He^*$, metastable excitation
(6) $He^* + 2He \rightarrow He_2^* + He$, Loss of He^* (He_2^* is not followed in the PIC)
(7) $He^* + N_2 \rightarrow e + N_2^+ + He$, Penning ionization by He^*
(8) $He^* + He \rightarrow He^* + He$, He^* elastic scattering.

The cross-sections for reactions (1), (2) and (5) are from the Morgan cross-section data from the LXcat internet database [21]. We chose the Morgan data set since it provided both the metastable and total excitation cross-sections for He, whereas the other data sets only provided the total excitation. The cross-sections for reactions (3), (6) and (7) are deduced from the reaction rate coefficients $K(T_e)$ in [18]: i.e. (i) if $K(T_e) = C_0 = \text{const}$, then $\sigma(v) = C_0/v$ and (ii) if $K(T_e) = B_0(T_g/T_e)^{1/2}$ with $B_0 = \text{const}$ and gas temperature T_g (in V) = const, then $\sigma(v) = (\pi e T_g/(2m_e))^{1/2} B_0/v^2$. The cross-section for reaction (4) is estimated using the N_2^+ mobility in He in [18]: $\mu_i = e/(m_{N_2} \nu_{mi}) = 2.28 \times 10^{-3}\,m^2\,V^{-1}\,s^{-1}$. Assuming a 760 Torr constant mobility discharge at $T_g = 0.026$ V, $K_{im} \equiv \nu_{im}/n_g = e/(n_g \mu_i m_{N_2}) = 6.17 \times 10^{-17}\,m^3\,s^{-1}$. This results in momentum transfer and total ion scattering cross-sections of $\sigma_{im}(v) = 6.17 \times 10^{-17}/v\,m^2$ and $\sigma_{it}(v) = [(m_{N_2} + m_{He})/m_{He}]\sigma_{im}(v) = 4.94 \times 10^{-18}/v\,m^2$, respectively. The cross-section for reaction (8) is estimated in a similar manner using the diffusion coefficient $D_{He^*} = eT_g/(m_{He}\nu_{He}) = 1.64 \times 10^{-4}\,m^2\,s^{-1}$ in [18], resulting in a total He^* scattering cross-section of $3.14 \times 10^{-16}/v\,m^2$. Figure 1 shows the PIC cross-sections versus incident particle energy $\mathcal{E}$ for (a) electron–neutral and electron–ion recombination collisions and (b) ion–neutral and metastable–neutral collisions. Note that to avoid infinite cross-sections at low incident energies when a cross-section $\sigma \propto 1/v \propto 1/\mathcal{E}^{1/2}$, we choose a cutoff energy $\mathcal{E}_c = 0.1$ eV for electrons and $\mathcal{E}_c = 0.01$ eV for metastables and ions such that the cross-section is a constant below $\mathcal{E}_c$.

A previous work [12] showed that for He/0.1%N_2 discharges, the dominant positive ion is N_4^+ rather than N_2^+. The N_4^+ ions are created by a helium-stabilized three-body association reaction, $N_2^+ + N_2 + He \rightarrow N_4^+ + He$, and are lost mainly by mobility-dominated flow to the walls. Since mobilities scale inversely with the square root of the reduced mass of the ion and background neutral, the mobilities and hence the loss rates of N_2^+ and N_4^+ in helium are practically the same. The association reaction then merely substitutes one ion for another, with no change in the basic discharge dynamics. At the highest input currents and powers, electron–ion recombination losses become important. The larger recombination rate coefficient for N_4^+ compared with N_2^+ [12] may lead to modifications of the discharge dynamics deep within the region of γ mode operation.

The time-averaged temperature profile T_j for each species at each grid point j is calculated by

$$T_j = \frac{1}{3e}\langle(\overline{v_x^2} - \overline{v_x}^2) + (\overline{v_y^2} - \overline{v_y}^2) + (\overline{v_z^2} - \overline{v_z}^2)\rangle. \quad (1)$$

Here, the angular brackets denote a time-average while the overlines denote averages over the particles weighted to grid point j.

For 1D symmetric parallel-plate rf discharges, the oscillating sheath edge positions for the sheaths at the two opposing walls have the same amplitude and rf period, but are 180° out of phase. At each timestep, the instantaneous sheath edge positions are determined by calculating the ratio of n_e/n_i, starting at the center of the discharge and proceeding toward each sheath region. For each sheath, the sheath edge position $s(t)$ is taken to be the position where $n_e/n_i = 1/2$. The maximum sheath width s_m is the maximum distance of the sheath edge $s(t)$ from the adjacent wall over an rf period.

2.2. PIC simulation results

Simulations were conducted for an rf capacitive atmospheric pressure ($p = 760$ Torr), room temperature ($T_g = 0.026$ V) He/N_2 discharge with a gap length $l = 1$ mm and plate area $A = 1\,cm^2$. We fixed the N_2 fraction at 0.1% and assumed an ion-impact secondary electron emission coefficient γ of 0.25 [14]. This value for γ is based on [14], taking into

account both the ions and the metastables. Since the global model (discussed in the next section) assumes a current source, the PIC simulations also use a current source to drive the discharge. The input rf current density amplitude was varied from $J = 400$ to $6000\,\mathrm{A\,m^{-2}}$. The applied rf frequency ranged from $f = 13.56$ to $40.68\,\mathrm{MHz}$. The global model in a previous work [18] showed that the sheath width s_m increases with decreasing frequency, so that narrow gap discharges are harder to maintain for lower frequencies where s_m approaches $l/2$. We chose an intermediate frequency of 27.12 MHz for the base case to avoid this limit.

The timestep Δt and the grid spacing Δx were chosen to satisfy the constraints listed above in section 2.1. For all the cases, we chose a timestep $\Delta t = 1.4 \times 10^{-13}\,\mathrm{s}$ in order to satisfy $\nu_\mathrm{max}\Delta t \ll 1$. The grid spacing Δx for each case was chosen so that $\Delta x \approx \lambda_\mathrm{D}$. For the low power, low density case of $J = 400\,\mathrm{A\,m^{-2}}$ at 27.12 MHz, $\Delta x = 10^{-5}\,\mathrm{m}$, whereas for the high power, high density case of $J = 6000\,\mathrm{A\,m^{-2}}$ at 27.12 MHz, $\Delta x = 8.3 \times 10^{-7}\,\mathrm{m}$. On a moderate 2.2 GHz CPU workstation with 8 GB of memory, the low-density case took about 3 h to reach convergence while the high density case took about 20 h.

Figures 2 and 3 show time-averaged PIC diagnostics for the base case and for 13.56 MHz, respectively. The left column shows the results for a low-power case at $J = 400\,\mathrm{A\,m^{-2}}$, and the right column shows the results for a high-power case at $J = 2000\,\mathrm{A\,m^{-2}}$. The diagnostics include the time-averaged charged particle and metastable densities and temperatures as well as the EEDF in the 'middle' and 'edge' regions of the discharge. We define the 'middle' as the region between $x = 0.4\,\mathrm{mm}$ and 0.6 mm and the 'edge' as the region between $x = 0$ and 0.2 mm. The 'edge' EEDF can be associated mainly with the hot-electron group in the sheaths while the 'middle' EEDF can be associated with the warm electron group in the bulk. The two dotted vertical lines denote the positions of the maximal sheath edge locations at $x = s_\mathrm{m}$ and $x = l - s_\mathrm{m}$, respectively. The PIC results for the collision rates (not shown) reveal that the He*-impact ionization of N_2 (i.e. Penning ionization) dominates over the electron-impact ionization of N_2 at both low and high powers and low and high frequencies. The high-energy tail of the EEDF above 20 eV is responsible for generating the He*, which in turn generates most of the ionization. Most of the ion flux is generated in the sheaths, and the ion flux Γ_s entering the sheath at $x = s_\mathrm{m}$ is much smaller than the ion flux Γ_w at the wall.

We see from figures 2 and 3 that the sheath widths increase with decreasing frequency and decreasing power. In figure 3(*a*), we see that s_m approaches $l/2 = 0.5\,\mathrm{mm}$ at $f = 13.56\,\mathrm{MHz}$ and $J = 400\,\mathrm{A\,m^{-2}}$. However, due to the high collisionality, the discharge can be maintained even in the absence of a quasi-neutral bulk region. At low powers, the electron temperature is fairly uniform, but the production of metastables is still mostly in the sheaths, as consistent with the comparison of EEDFs for the 'middle' and 'edge' electrons in figure 2(*e*). When comparing the low-power density profiles in figure 2(*a*) with those in figure 3(*a*), we see that the sheaths are smaller in the 27.12 MHz case compared with the 13.56 MHz case, but the charged particle densities are quite similar. There is an increase in absorbed power from $S_\mathrm{abs} = 1240$ to $1830\,\mathrm{W\,m^{-2}}$ as the frequency is decreased from 27.12 to 13.56 MHz for $J = 400\,\mathrm{A\,m^{-2}}$. The metastable densities are larger at 13.56 MHz, as will be explained by the balance equations in section 3. The Penning ionization is larger at 13.56 MHz due to the balance against larger wall losses. The ratio $\Gamma_\mathrm{s}/\Gamma_\mathrm{w}$ (not shown) is smaller at 13.56 MHz compared with 27.12 MHz, indicating less charged particle production in the plasma core at the lower frequency.

As seen in figures 2(*d*) and 3(*d*), at higher powers, the electron temperature drops in the bulk region and the warm bulk electrons become much cooler than the hot sheath electrons. In the high-power regime, the discharge is maintained by the hot sheath electrons, as the warm bulk electrons become too cold to create metastables. The avalanche multiplication of electrons in the sheaths concentrates the metastable densities in the sheath regions where the electrons are hot enough to excite the He atoms. Also, the higher electron and ion densities in the quasi-neutral core lead to increased electron–ion recombination, accounting for the dip in the densities toward the center. Comparing the high-power density profiles in figure 2(*b*) with those in figure 3(*b*), the profiles are similar but the density at 27.12 MHz is roughly half that at 13.56 MHz. This is mainly due to the higher T_e at 27.12 MHz, as will be explained in section 3. The effects of both electron multiplication in the sheaths and electron–ion recombination in the core are clearly in evidence. We note from the EEDFs in figures 2(*e*) and (*f*) that the tails of the distributions, which are the dominant source of the He* generation, are in the sheath regions. This fact will be important in the model construction.

Figure 4 shows 2D contour plots of the rates for electron-impact excitation of He to He* (metastable excitation) and He*-impact ionization of N_2 (Penning ionization) for the base case of 27.12 MHz. The vertical axis shows the spatial variation across the gap while the horizontal axis shows the time variation over an rf period. The left and right columns show the results for the low and higher power, respectively. In figure 4(*a*), we see that the metastables are created when and where the electron density and temperature are both high. The metastables created in figure 4(*a*) provide the ionization source in figure 4(*c*). The metastable excitation is localized in time while the Penning ionization is nearly uniform in time because the metastable lifetime is much longer than the rf period. In figure 4(*b*), the higher sheath field and lower bulk electron temperature at higher current (power) move most of the electron excitation to within the sheath regions. The electric field profiles over half an rf period, corresponding to the low- and high-power cases shown in figures 4(*a*) and (*b*) are shown in figure 5(*a*) and (*b*), respectively. At low powers, the maximum bulk field is about 1/3 of the maximum field at the wall while at high powers, the bulk field is small due to the high density. This effect is captured by the previous global model [18] and has been discussed in [16]. The implication is that even at the lowest power in the base case, most of the metastable production corresponds spatially to the high-field sheath regions.

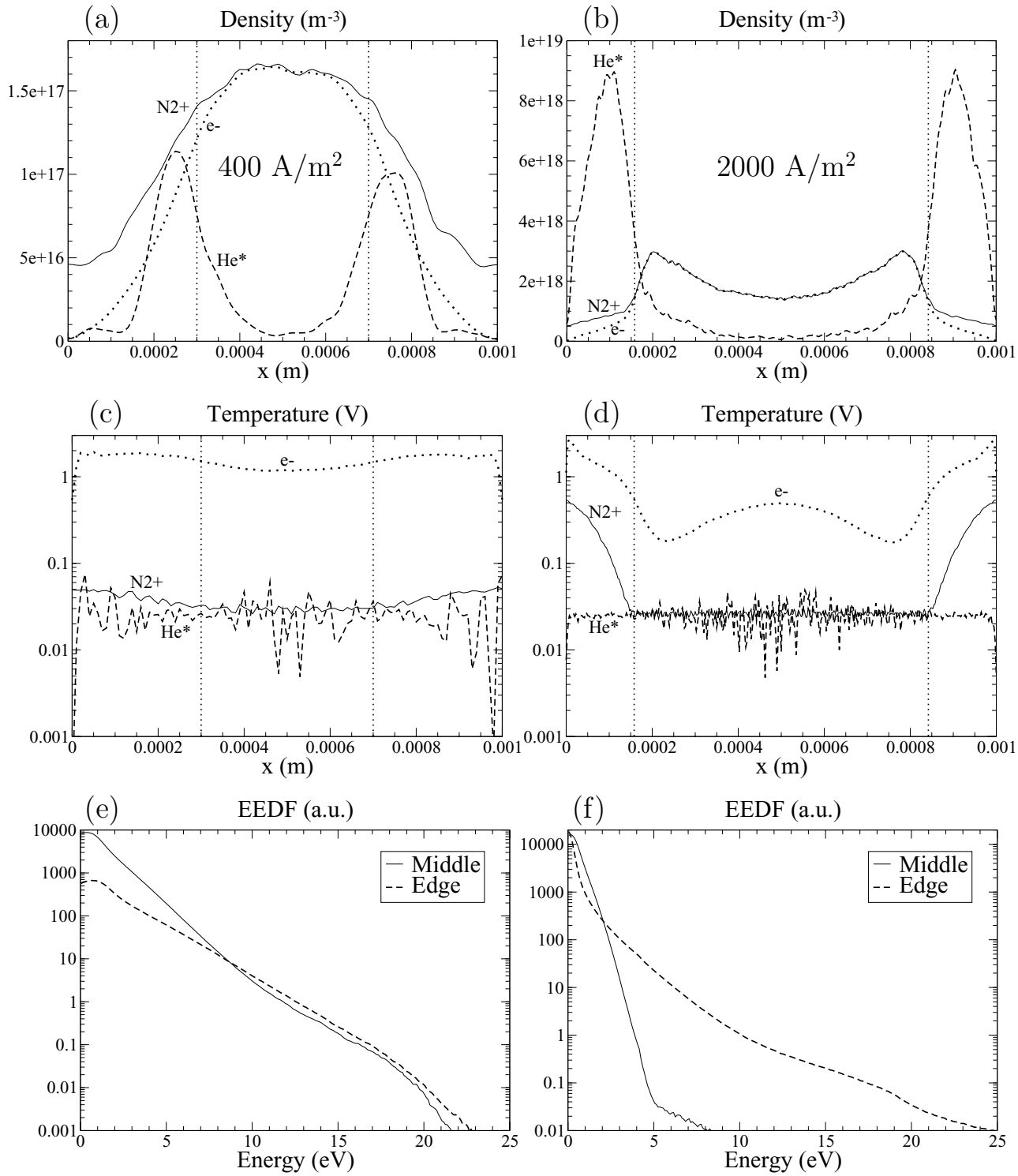

Figure 2. Time-averaged PIC results at 27.12 MHz, showing particle densities and temperatures, as well as the EEDF in the 'middle' ($0.4\,\text{mm} < x < 0.6\,\text{mm}$) and 'edge' ($0 < x < 0.2\,\text{mm}$) regions of the discharge. The left and right columns show the results for $J = 400\,\text{A m}^{-2}$ and $2000\,\text{A m}^{-2}$, respectively. The dotted vertical lines are at $x = s_\text{m}$ and $x = l - s_\text{m}$.

3. Two temperature homogeneous discharge model

In this section, we extend the previous homogeneous discharge model [18] to incorporate two electron components: warm electrons created in the low-field discharge region and hot electrons created in the high-field sheath region. A summary of the previous model is given in appendix A. The hot-electron energy relaxation length is $\lambda_\epsilon = (\lambda_\text{elas}\lambda_\text{inel}/3)^{1/2}$, with λ_elas and λ_inel the elastic and inelastic electron–neutral mean free paths. A typical hot electron has λ_ϵ of order $50\,\mu$m, much smaller than the typical gap size ($l \sim 1\,$mm). Therefore, hot electrons created in the sheath do not significantly penetrate

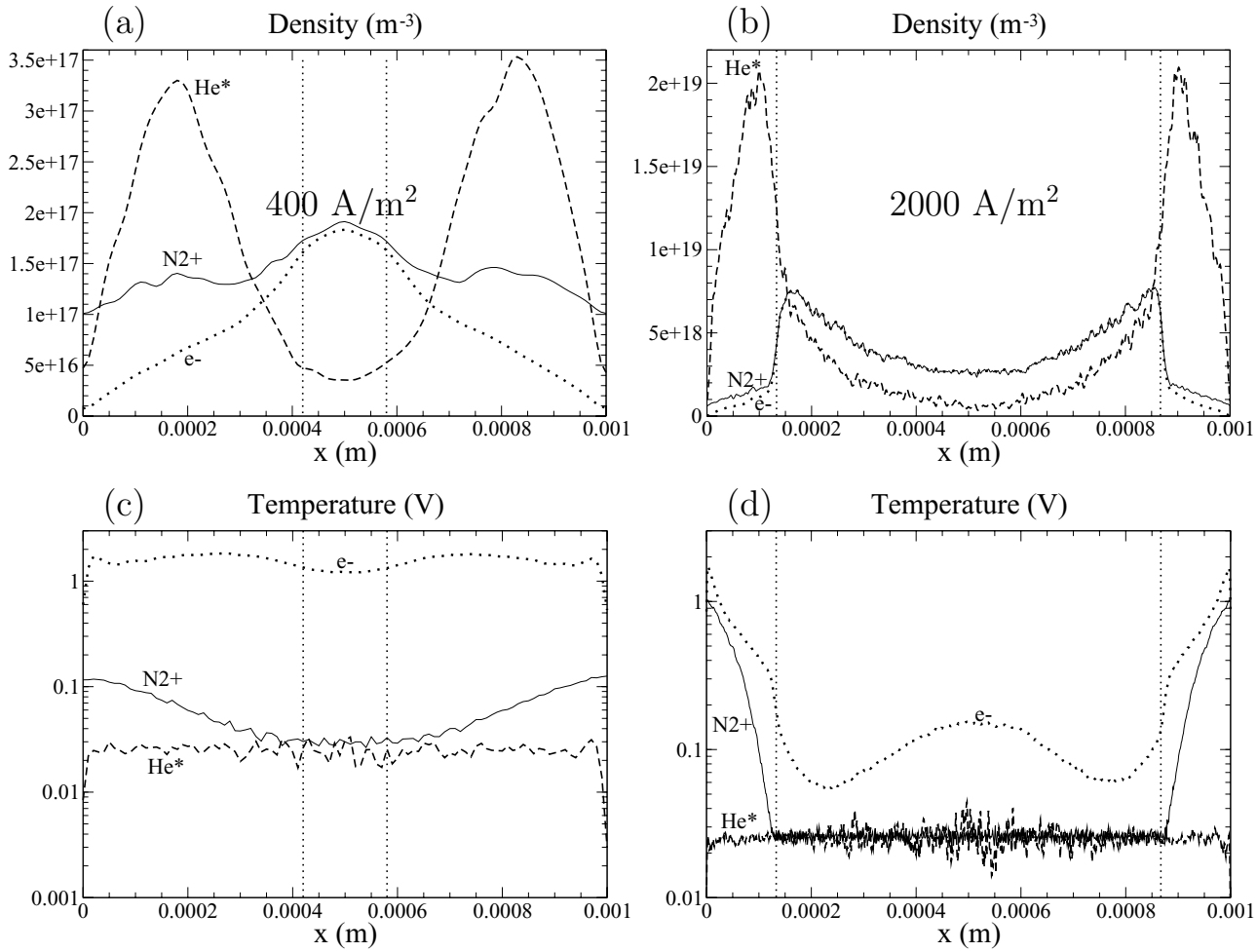

Figure 3. Time-averaged PIC results at 13.56 MHz, showing particle densities and temperatures. The left and right columns show the results for $J = 400\,\mathrm{A\,m^{-2}}$ and $2000\,\mathrm{A\,m^{-2}}$, respectively. The dotted vertical lines are at $x = s_\mathrm{m}$ and $x = l - s_\mathrm{m}$.

into the central plasma region. Since the metastable creation depends mainly on the hot component, the metastable density is taken to be within the sheath regions, as confirmed by the PIC simulations.

3.1. Two-temperature model assumptions

The assumptions are the following.

(a) The positive ion density n_i is uniform over the gap width l in the equilibrium model, except when determining the wall flux in (f).

(b) The electron density is equal to n_i over a 'cloud' width $d = l - s_\mathrm{m}$, and the maximum sheath width in the homogeneous model is $s_\mathrm{m} = 2J/(e\omega n_\mathrm{i})$ with ω the radian frequency.

(c) There are two electron populations: a uniform warm component (density n_e, temperature T_e), produced in the low-field region of the discharge within the oscillating electron cloud, and a small hot component (temperature $T_\mathrm{h} > T_\mathrm{e}$), produced in the high-field sheath regions exterior to the oscillating cloud. The hot component density n_h (averaged over the width of the cloud) is assumed to be much smaller than n_e.

(d) The fields and sheath oscillation are determined using the homogeneous model [18].

(e) Two helium metastable density profile models are examined. In both cases, the metastable density is assumed to be zero within the bulk plasma and equal to n_m0 at the sheath edges ($x = s_\mathrm{m}$ and $x = l - s_\mathrm{m}$). Then, the metastable density is either uniform in the sheath regions or falls linearly to zero at the walls. The average metastable density (over the gap width l) is then either $n_\mathrm{m} = 2\,n_\mathrm{m0} \cdot (s_\mathrm{m}/l)$ or $n_\mathrm{m} = n_\mathrm{m0} \cdot (s_\mathrm{m}/l)$, respectively.

(f) The ion flux Γ_w lost to a wall is determined from a constant mobility rf CL that includes the uniform or triangular ion source profiles within the sheath; a collisional Bohm criterion [22] is used to join the sheath to the plasma.

(g) The oscillating temperature $T_\mathrm{e}(t)$ of the warm component is determined by equating the ohmic power to the collisional losses, using the Maxwellian elastic and inelastic rate coefficients for the warm electrons [18].

(h) The oscillating hot component temperature $T_\mathrm{h}(t)$ is found from a kinetic calculation [23], using the space- and time-varying sheath electric field. The hot electrons are also assumed to have a sinusoidally oscillating temperature $T_\mathrm{h}(t)$, in general different from (and larger than) the

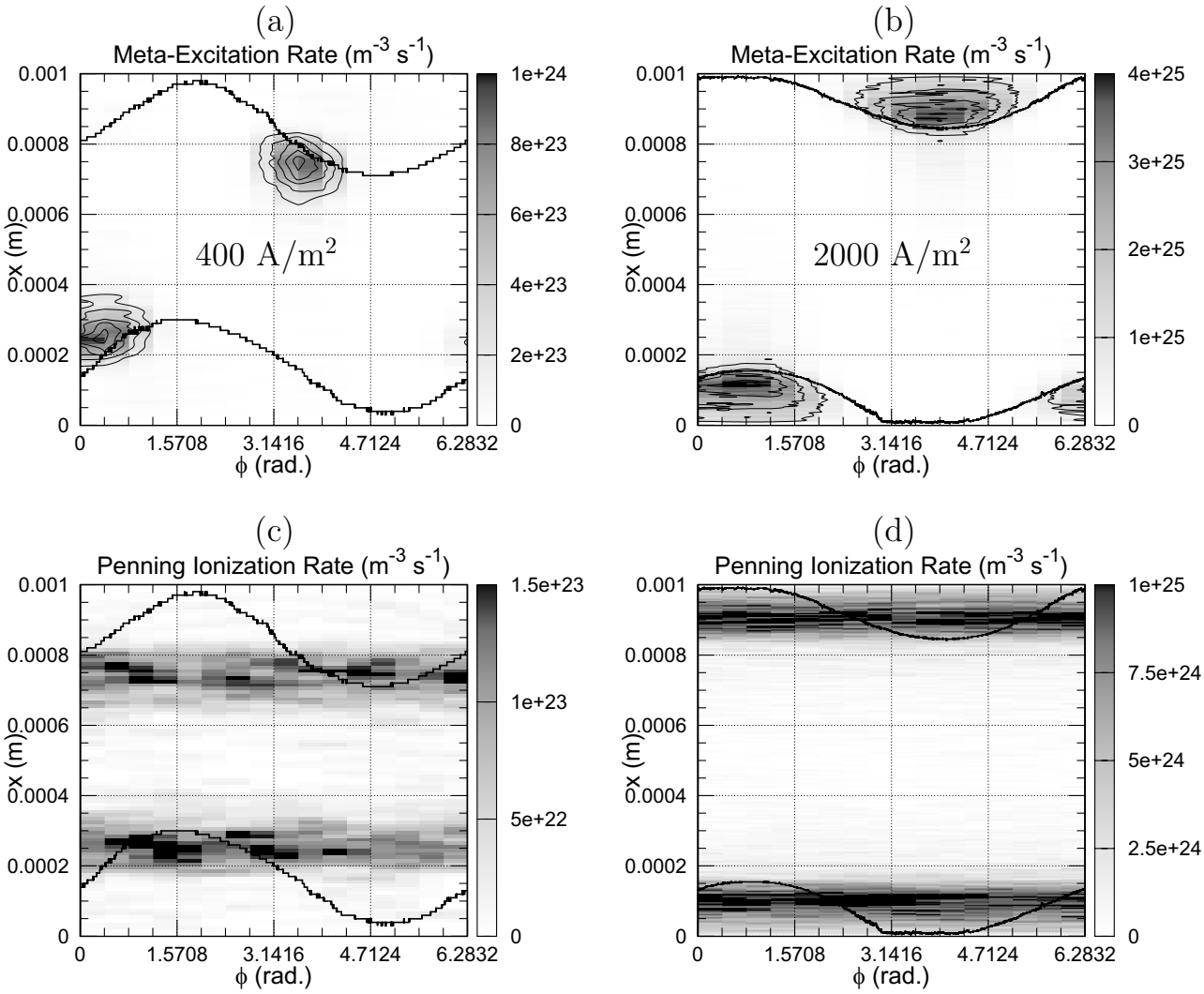

Figure 4. 2D contour plots at 27.12 MHz, showing metastable excitation and Penning ionization rates with space and time variation shown on the vertical and horizontal axes respectively. The left and right columns show the results for $J = 400\,\mathrm{A\,m^{-2}}$ and $2000\,\mathrm{A\,m^{-2}}$, respectively. The dark solid curves show the sheath edge positions at the opposing walls.

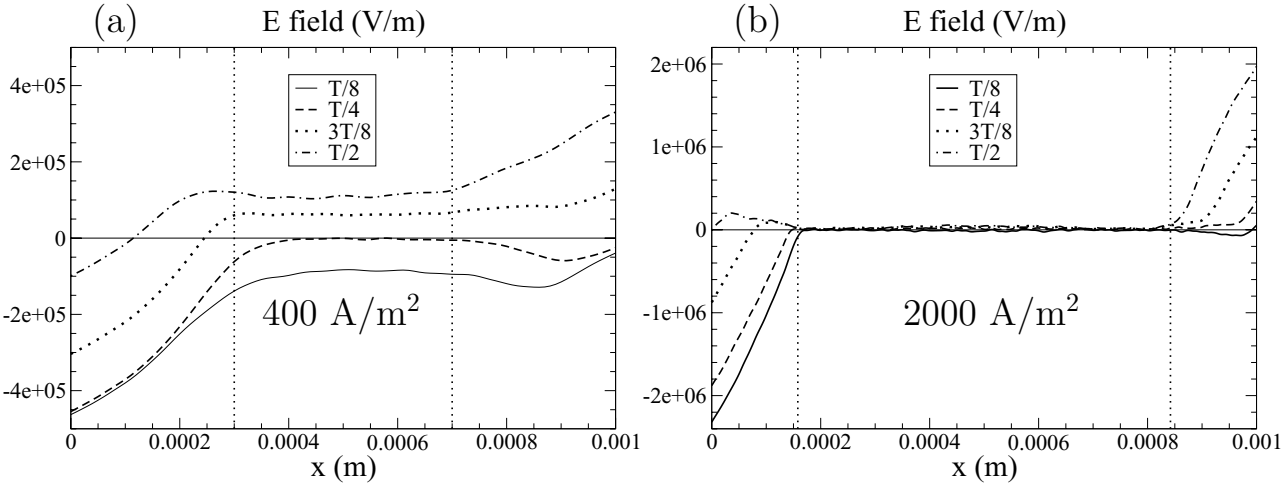

Figure 5. PIC results at 27.12 MHz, showing the electric field at four times during a half period for (*a*) $J = 400\,\mathrm{A\,m^{-2}}$ and (*b*) $J = 2000\,\mathrm{A\,m^{-2}}$. The dotted vertical lines are at $x = s_\mathrm{m}$ and $x = l - s_\mathrm{m}$.

sinusoidally oscillating temperature $T_e(t)$ of the warm electrons.

(i) The time-average rate coefficients for the warm and hot activated electron reactions are found by averaging over the oscillating temperatures. The electron-activated reaction rates from the two classes of electrons are summed to determine the total reaction rates used in the particle balance equations.

(j) The multiplication factors M_γ for ionization by secondary electrons and M_P for Penning ionization in the sheath are calculated using the homogeneous model expressions for the time-varying sheath motion and the space- and time-varying electric fields.

3.2. Model equations

The hot component density is determined from the hot-electron balance. Because the Penning ionization rate is slow compared with the rf frequency, only the part of the Penning ionization that occurs in the time-varying high-field region of the sheath, and their multiplication products, result in the production of hot electrons. All of the secondary electrons, and their multiplication products, are taken to be hot. With these assumptions, the equilibrium hot-electron balance is

$$(M_P - f_e)K_P n_m n_{N_2} l + 2\gamma M_\gamma \Gamma_w = (K_{hiz} n_{N_2} + K_{hm} n_{He} + K_{hi} n_i) n_h d, \quad (2)$$

where K_P is the Penning ionization rate coefficient, f_e is the Penning fraction produced in the time-varying low-field region of the sheath, γ is the secondary electron emission coefficient from the walls, K_{hiz} and K_{hm} are the hot-electron ionization and metastable excitation rate coefficients, and K_{hi} is the hot electron–ion recombination rate coefficient. We use $f_e = 1/2$, because the low-field electron cloud penetrates into the sheath region half the time for the homogeneous model. The two terms on the left-hand side give the hot-electron production due to Penning ionization and secondary electron creation, respectively, including their multiplication products. The terms on the right-hand side give the loss of hot electrons to the colder component by ionization, metastable production and recombination. With the rate coefficients determined from the average electric fields in the high-field sheath regions, (2) determines the hot density n_h in terms of the other variables.

The positive ion balance is

$$l\frac{dn_i}{dt} = 2\gamma(M_\gamma - 1)\Gamma_w + M_P K_P n_m n_{N_2} l + K_{hiz} n_h n_{N_2} d + K_{iz} n_e n_{N_2} d - 2\Gamma_w - K_{ei} n_i n_e d - K_{hi} n_h n_i, \quad (3)$$

where K_{iz} is the warm electron ionization rate coefficient, and K_{ei} is the warm electron–ion recombination coefficient. The first and second terms on the right-hand side give the ion creation due to secondary creation and Penning ionization, including their multiplication products. The third and fourth terms give the direct ionization, and the fifth, sixth and seventh terms give the wall losses and the electron–ion recombination losses.

The helium metastable balance is

$$l\frac{dn_m}{dt} = (K_m n_e + K_{hm} n_h) n_{He} d - K_P n_m n_{N_2} l - K_3 n_m n_{He}^2 l - 12 D_m n_m / l, \quad (4)$$

with K_3 the rate coefficient for metastable loss due to three-body recombination and D_m the metastable diffusion coefficient for loss to the walls.

The wall flux Γ_w is determined from an ion transport model. In previous work [18, 24] we used $\Gamma_w = \mu_i n_{iw} E_w$, with μ_i the ion mobility, n_{iw} the ion density at the wall and E_w the time-average electric field at the wall. Based on fluid simulation results, we chose a reasonable, but somewhat arbitrary, wall density $n_{iw} = n_i/2$. In this work, we calculate the wall flux self-consistently from a collisional CL rf sheath model, including a source of ions within the sheath. Joining this sheath solution to the bulk plasma at the plasma–sheath edge, determined from a modified Bohm condition, yields the flux (appendix B, equation (B16))

$$\Gamma_w = 0.56\,\mu_i E_s^{1/6} E_w^{5/6} n_{is}, \quad (5)$$

where $E_s = T_e/N\lambda_{Ds}$ and $E_w = J/\omega\epsilon_0$ are the time-average electric fields at the joining position and at the wall, respectively, with λ_{Ds} the electron Debye length at the joining position, and $n_{is} = n_i$, the ion density in the homogeneous model. As discussed in appendix B, the Bohm sheath coefficient is chosen to be $N = 5$. This corresponds to the E_s values seen in the PIC simulations, but the results are not sensitive to the particular choice since Γ_w is a weak function of E_s in (5). Substituting for Γ_w, together with the definitions of E_s and E_w, from (5), into (2) and (3), and using (2) to eliminate n_h from (3) and (4), we have two equations to be solved for the equilibrium densities n_i and n_m, once the reaction rates and multiplication factors are known.

3.3. Hot electron and multiplication dynamics

To find the time- and space-averaged hot-electron temperature and rate coefficients, we use a Bolsig+ kinetic calculation [23] for the He/N_2 mixture with the Morgan cross section set [21] to determine the ionization rate coefficient K_{hiz}, the metastable excitation rate coefficient K_{hm}, the mean electron energy $\mathcal{E}_e$, and the first Townsend coefficient α as a function of E/n_g, with n_g the gas density. The quantity $K_{hiz}n_{N_2} + K_{hm}n_{He}$, the sum of the hot-electron loss frequencies to the background gas, appears on the right-hand side of the hot electron balance (2). Introducing an effective rate coefficient

$$K_{eff} = K_{hiz} + K_{hm} n_{He}/n_{N_2}, \quad (6)$$

we first determine a fit to K_{eff} as a function of E/n_g in Td ($1\,\mathrm{Td} = 10^{-21}\,\mathrm{V\,m^2}$) for the typical fields present in the high-field sheath regions and for the specific fractions (0.1% and 0.3%) of the minority N_2 species. From the Bolsig+ calculation, a good fit for $10 \lesssim E/n_g \lesssim 300\,\mathrm{Td}$ is found to be a power law $K_{eff} = B_{eff}(E/n_g)^q$. For $He/0.1\%N_2$, $B_{eff} = 7.50 \times 10^{-17}$ and $q = 1.975$; for $He/0.3\%N_2$, $B_{eff} = 1.206 \times 10^{-17}$ and $q = 2.12$.

Next we do the space averaging. The peak time-varying electric field in the sheath at the wall is

$$E_{peak} = \frac{J}{\omega\epsilon_0}\left(1 + \frac{1}{\sqrt{(1 + 1/\kappa_l^2)}}\right), \quad (7)$$

where J is the rf current density and κ_I (see appendix A) is the imaginary part of the plasma relative dielectric constant. Within a homogeneous sheath, $E \propto x$, and the space-average of $K_{\rm eff}$ over the oscillating sheath gives

$$\overline{K}_{\rm eff}(\omega t) = K_{\rm eff}(\omega t, \text{wall}) \cdot \frac{1}{s(\omega t)} \int_0^{s(\omega t)} \left(\frac{x}{s(\omega t)}\right)^q \mathrm{d}x = \frac{K_{\rm eff}(\omega t, \text{wall})}{q+1}. \quad (8)$$

Letting $\overline{K}_{\rm eff} = B_{\rm eff}(E_{\rm max}/n_{\rm g})^q$ and $K_{\rm eff,peak} = B_{\rm eff}(E_{\rm peak}/n_{\rm g})^q$, then from (8), we can solve for the space-averaged maximum (in time) electric field $E_{\rm max}$ in terms of $E_{\rm peak}$, obtaining $E_{\rm max} = E_{\rm peak}/(q+1)^{1/q}$.

Introducing $T_{\rm hmax} = 2\mathcal{E}_{\rm e}/3$, we obtain a good fit to an Arrhenius form $\overline{K}_{\rm eff} = A_{\rm eff}\exp(-C_{\rm eff}/T_{\rm hmax})$. Inverting this yields the space-averaged maximum (with respect to time) temperature of the hot electrons in the high-field sheath region. For the time-averaging, we assume that the sheath electron temperature $T_{\rm h}$ oscillates sinusoidally in time, with a maximum value $T_{\rm hmax}$ and a minimum value of near zero. Therefore, we calculate the time-average effective rate coefficient $\langle K_{\rm eff}\rangle$ for the hot electrons in the usual way [18]

$$\langle K_{\rm eff}\rangle = A_{\rm eff}\,\mathrm{erfc}\left(\sqrt{C_{\rm eff}/T_{\rm hmax}}\right), \quad (9)$$

as done for the warm electrons (appendix B, equation (A11)). Using (9) in (2), we solve for the density $n_{\rm h}$ (averaged over the cloud width d) of the hot electrons. Using $T_{\rm hmax}$, we determine all the time-average hot-electron rate coefficients. Note that the rf and dc components of the sheath field were not separately used in the Bolsig+ calculations.

We determine the secondary electron and Penning multiplication factors M_γ and $M_{\rm P}$ using a fit to the first Townsend coefficient $\alpha(x,t)$, which is the number of electron–ion pairs generated per meter by the multiplication process [25]. We use a fitting function that works over a wide $E/n_{\rm g}$ range [26, p 56]

$$\alpha = An_{\rm g}\exp\left(-B(n_{\rm g}/E)^{1/2}\right). \quad (10)$$

The results for He/0.1%N_2 are $A = 2.3916\times10^{-20}\,\mathrm{m}^2$ and $B = 27.6142\,\mathrm{Td}^{1/2}$ for $10 < E/n_{\rm g}\,(\mathrm{Td}) < 300$.

The space- and time-average secondary electron multiplication factor can be written as

$$M_\gamma = \left\langle \exp\int_0^{s(t)} \alpha(x',t)\,\mathrm{d}x' \right\rangle_{\omega t}, \quad (11)$$

where $x' = 0$ at the wall and $x' = s_{\rm m}$ at the plasma–sheath edge. The sheath oscillation $s(t)$ and the sheath electric field $E(x,t)$ are found from the homogeneous discharge model solution (appendix A, equations (A2) and (A3)). Substituting (A3) into (10), and then (10) and (A2) into (11), we determine M_γ as a function of $n_{\rm e}$ and $s_{\rm m}$. The integrations in (11) are done numerically. The electron density and maximum sheath width are determined from the homogeneous model sheath equations during integration of the differential equations for the particle balances in the discharge. The distributed Penning source in the sheath leads to a more complicated expression for the Penning multiplication factor

$$M_{\rm P} = \frac{1}{s_{\rm m}}\left\langle \int_0^{s(t)} \mathrm{d}x'\,G(x')\exp\left[\int_{x'}^{s(t)} \mathrm{d}x''\,\alpha\big(E(x'',t)\big)\right]\right\rangle_{\omega t}, \quad (12)$$

where the normalized source distribution is $G(x') = 2$ for a uniform profile and $G(x') = 16x'/3$ for a triangular profile that falls to zero at the wall.

Again the integrations are done numerically. Note that the no-multiplication condition is $M_\gamma = M_{\rm P} = 1$.

3.4. Collapse of the warm temperature

A notable feature of the PIC results is the transition from a relatively high temperature in the plasma bulk at low rf currents to a strongly depressed temperature at high currents. This collapse of the electron temperature in the central discharge core is analogous to the traditional α to γ mode transition [25] in low-pressure discharges, but the main mechanism is Penning ionization rather than secondary emission. At high currents the hot-electron multiplication processes in the high-field time-varying sheath region replace the warm electron Penning production in the low-field cloud, thus supplying the required ion wall losses. To see this we use a simplified model neglecting small terms in the particle balances, including direct ionization, electron–ion recombination, metastable diffusion to the walls, and three-body metastable loss. The hot-electron temperature $T_{\rm h}$ is set by the sheath electric field, which from (7) scales as $E \sim J/\omega\epsilon_0$. Letting $f_{\rm e}$ be the fraction of the Penning ionization within the low-field electron cloud, then from (2) the hot-electron balance is

$$(M_{\rm P} - f_{\rm e})K_{\rm P}n_{\rm m}n_{\rm N_2}l + 2M_\gamma\gamma\Gamma_{\rm w} = K_{\rm hm}n_{\rm h}n_{\rm He}d. \quad (13)$$

The ion balance is given from (3)

$$2\gamma(M_\gamma - 1)\Gamma_{\rm w} + M_{\rm P}K_{\rm P}n_{\rm m}n_{\rm N_2}l = 2\Gamma_{\rm w}. \quad (14)$$

The metastable balance is given from (4)

$$K_{\rm P}n_{\rm m}n_{\rm N_2}l = (K_{\rm m}n_{\rm e} + K_{\rm hm}n_{\rm h})n_{\rm He}d. \quad (15)$$

Substituting $K_{\rm hm}n_{\rm h}n_{\rm He}d$ from (13) into (15), we obtain

$$(1 + f_{\rm e} - M_{\rm P})K_{\rm P}n_{\rm m}n_{\rm N_2}l - 2\gamma M_\gamma\Gamma_{\rm w} = K_{\rm m}n_{\rm e}n_{\rm He}d. \quad (16)$$

Solving this for $K_{\rm P}n_{\rm m}n_{\rm N_2}l$ and substituting into (14), we obtain

$$K_{\rm m}n_{\rm e}n_{\rm He}d = 2\Gamma_{\rm w}\left[\frac{(1 + f_{\rm e} - M_{\rm P})(1 + \gamma - \gamma M_\gamma)}{M_{\rm P}} - \gamma M_\gamma\right]. \quad (17)$$

Since (5) shows that $\Gamma_{\rm w} \propto n_{\rm e}$ to a good approximation (except for the weak dependence of $\Gamma_{\rm w}$ on $\lambda_{\rm Ds}$ through $E_{\rm s}^{1/6}$, which makes $\Gamma_{\rm w}$ actually scale as $n_{\rm e}^{13/12}$), the $n_{\rm e}$ dependences on the left and right sides of (17) cancel. If the term in square brackets is set to zero, then warm electron ionization is no longer required to maintain the plasma, leading to the collapse

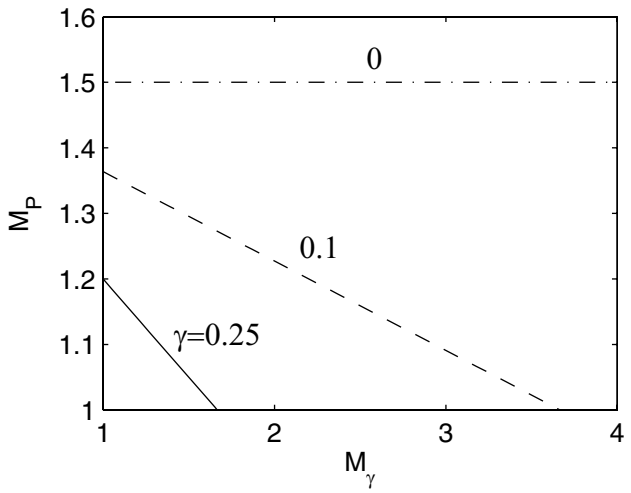

Figure 6. Penning multiplication factor M_P versus secondary electron multiplication factor M_γ for $\gamma = 0.25$ (solid), 0.1 (dashed) and 0 (dashed–dotted). Above each line, warm electron ionization is not required to sustain the plasma, indicating the transition for the collapse of the warm electron temperature for each γ value.

of T_e. Setting this term to zero and solving for M_P, we obtain the condition

$$M_P = \frac{1+\gamma-\gamma M_\gamma}{1+\gamma}(1+f_e). \tag{18}$$

For $\gamma \to 0$, we find $M_P = 1 + f_e$; i.e. the multiplication must replace the bulk fraction f_e of the Penning ionization in the discharge. For the homogeneous model with $f_e = 1/2$, we have $M_P = 3/2$. The condition (18) is plotted in figure 6 for the homogeneous model assumptions $f_e = 1/2$ and $\gamma = 0$, 0.1 and 0.25. The PIC simulations for the base case also show $f_e \approx 1/2$ at the transition.

Because the first Townsend coefficient α in (10), which determines the multiplication factors in (11) and (12), depends strongly (exponentially) on the peak sheath electric field given in (7), the condition (18) for the α to γ transition and collapse of the warm T_e occurs at a particular value of $E_{peak} = E_{peak,T}$ and weakly depends on other discharge parameters. Since for $|\kappa_I| \gg 1$ we find from (7) that

$$\left(\frac{2J}{\omega\epsilon_0}\right)_T \approx E_{peak,T}, \tag{19}$$

From (19), we expect that the transition value of J is proportional to the rf frequency, which we will see in section 4.

In the α mode with $M_P \approx 1$ and setting $\gamma = 0$, we can solve (13) and (15) for the ratio n_h/n_e, obtaining

$$\frac{n_h}{n_e} = \frac{K_m}{K_{hm}}\frac{1-f_e}{f_e}. \tag{20}$$

Setting $f_e = 1/2$, for T_h significantly greater than T_e, $n_h \ll n_e$ since K_m and K_{hm} are exponentially dependent on temperature. However, the total production of metastables by the hot and warm electrons is comparable since $K_{hm}n_h \approx K_m n_e$ for $f_e \approx 1/2$.

3.5. Electron power balance and CL sheath

The ohmic heating of the warm component dominates the total electron energy absorption, which is balanced almost entirely by the elastic scattering energy loss against the neutral helium. The warm electron power balance is then found from (A10), assuming that the inelastic losses are small ($\zeta \approx 1$ in equation (A8)). Inserting $|\kappa_I| = \omega_p^2/\omega\nu$ and $\kappa_R \approx 1$ into (A10), we obtain

$$n_e^2 T_e = \frac{m_{He}}{6\,e^3}J^2 - \left(\frac{\epsilon_0 m_e \omega\nu}{e^2}\right)T_e. \tag{21}$$

The second term on the right-hand side can be important at low currents and high frequencies, as will be seen in the next section; it essentially represents a phase shift between J and E [16]. However, in most cases, we have the simpler result

$$n_e^2 T_e = \frac{m_{He}}{6\,e^3}J^2, \tag{22}$$

showing that n_e scales as $1/\sqrt{T_e}$ at fixed current, independent of frequency. As the rf current is increased, the collapse of T_e through the α to γ transition then leads to a greater than linear increase in density with current. Before the collapse, the warm temperature T_e is roughly constant as the rf current increases. Then (22) gives the scaling $n_e \propto J$. In the transition region of the collapse, T_e rapidly decreases, and n_e then increases more rapidly than linearly with J, as seen in the PIC simulations. Finally, deep within the collapse region, we would expect that $T_e \approx$ const, perhaps set by the background gas temperature or hot-to-warm electron energy transfer processes. We would then again expect to see $n_e \propto J$, but with a different (larger) constant of proportionality. This behavior is clearly seen for the standard case in figure 7(*b*).

Although the maximum sheath width $s_m = 2J/(e\omega n_i)$ is used in the homogeneous model to determine the discharge dynamics and electric fields (see appendix A), the PIC simulations indicate that the sheath has a CL structure, with significant generation of ion flux within the sheath (see appendix B). The product of CL sheath width s_{CL} and wall flux Γ_w is found from (B7) to be

$$s_{CL}\Gamma_w = K_{CL}\frac{\mu_i J^2}{e\omega^2\epsilon_0}, \tag{23}$$

where Γ_w is given in (5) and K_{CL} is a constant which depends on the ion source profile. $K_{CL} = 3/2$ or 9/8 for a uniform or triangular ion source profile in the sheath, and $K_{CL} = 3/4$ when all ions enter at the plasma–sheath edge (no ion source within the sheath). The factor of 2 change in K_{CL} indicates a corresponding sensitivity of the equilibrium results to the ion source profile, as will be found and further discussed in the next section.

4. Comparison of PIC and model results

In this section we compare the space- and time-averaged PIC results to those obtained from the hybrid two-temperature homogeneous discharge model. In the first subsection, we examine the variation with rf current, spanning the space from a low current of 400 A m^{-2}, where there is very little

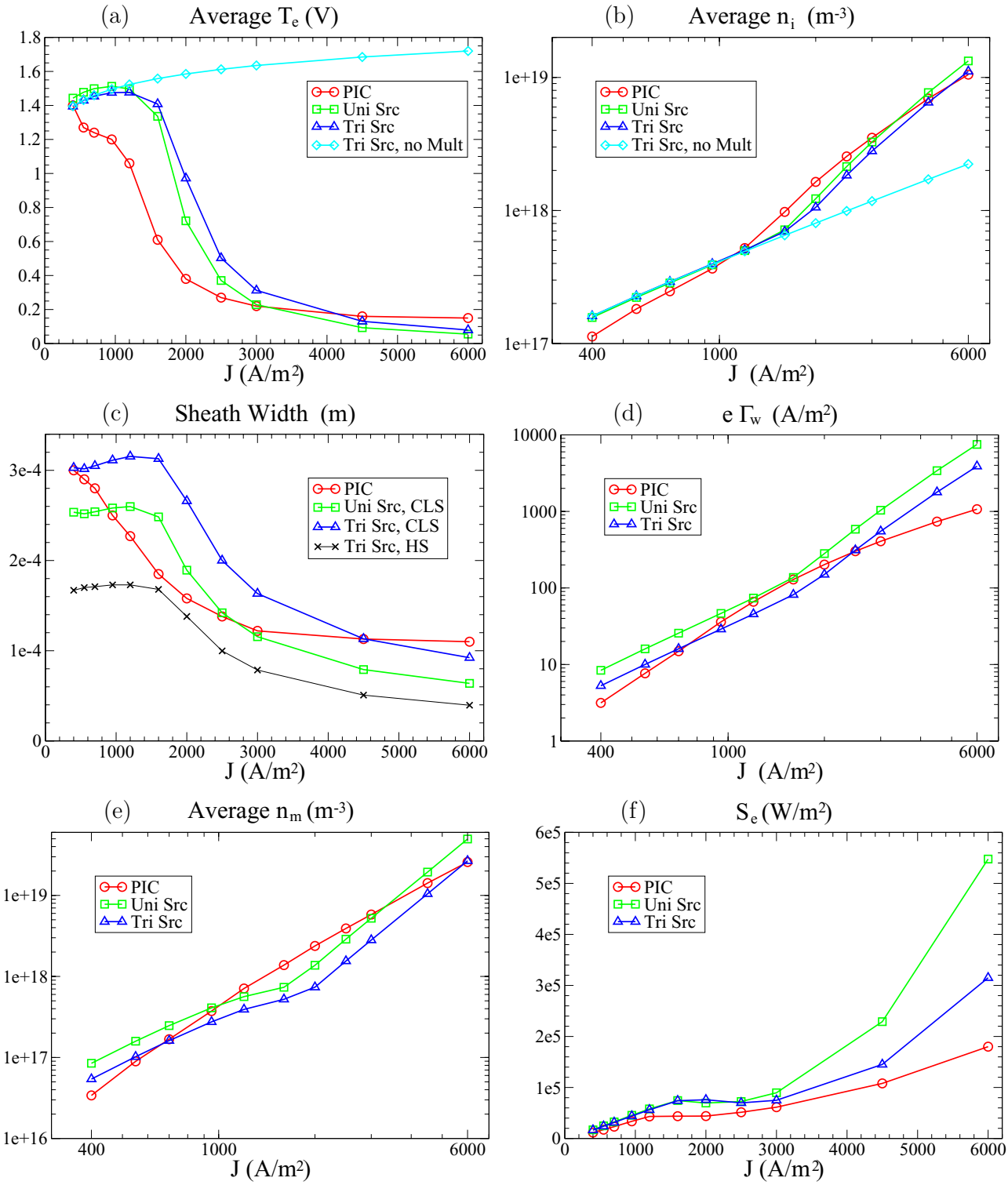

Figure 7. Comparison of results at 27.12 MHz for PIC (circles) and theory with a uniform (squares) or triangular (triangles) ion source for $J = 400$–$6000\,\mathrm{A\,m^{-2}}$, showing (*a*) average T_e (V), (*b*) average n_i ($\mathrm{m^{-3}}$), (*c*) sheath width (m), (*d*) ion wall current $e\Gamma_w$ ($\mathrm{A\,m^{-2}}$), (*e*) average n_m ($\mathrm{m^{-3}}$) and (*f*) electron power flux S_e ($\mathrm{W\,m^{-2}}$). (*a*) and (*b*) show theory results with multiplication turned off (diamonds). (*c*) also shows the maximum sheath width for a homogeneous sheath (crosses).

multiplication in the sheaths to $6000\,\mathrm{A\,m^{-2}}$ with significant multiplication. This spans the range from a situation in which the warm electron component in the bulk plasma plays a significant role in supporting the helium metastable excitation, to a situation in which sufficient sheath multiplication occurs to cause the warm temperature to drop to a low value at which it plays no significant role in the excitation process. In the second subsection, we examine the variation with the driving frequency, spanning the range from 13.56 to 40.68 MHz. Some results with He/0.3%N_2 are discussed, both in order to examine the scaling with trace gas percentage, and as the experimentally interesting range of 0.1–0.3%N_2 maximizes

the atomic nitrogen production [27, 28]. The PIC values for the globally averaged T_e in this section are obtained by using the $T_e(x)$ profiles from section 2 and performing the following particle-weighted average:

$$T_e = \frac{\int_0^l n_e(x) T_e(x)\, dx}{\int_0^l n_e(x)\, dx}. \quad (24)$$

4.1. Variations with rf current

In figure 7 we compare the PIC (circles) to the model for the triangular source of He^* in the sheath (triangles) and for a uniform source (squares). In figure 7(*a*) we show a density-weighted average T_e. The model indicates, as expected, a relatively constant T_e, where condition (18) that multiplication suppresses the temperature of the warm electrons is not satisfied. This is followed by a rapid decrease in the temperature with increasing J; i.e. as M_P and M_γ become increasingly important. The average T_e in the PIC falls more gradually, but begins almost at the lowest rf currents, resulting from a complex set of effects, that can be qualitatively understood from the PIC profiles in figures 2 and 3. In the model, if the multiplication is shut off, T_e (diamonds) follows the same path from low J's up to the highest J's, confirming that the drop in T_e results from the multiplication. The consequence for the average $n_i \approx n_e$ is seen in figure 7(*b*), which from (22) indicates that $n_i \propto J$ if T_e is constant, but n_i increases faster in the transition region where T_e is falling. Then n_i resumes the linear scaling at the highest currents, where T_e is again constant but at a low value. As expected, if the multiplication is shut off in the model, the low J linear scaling of n_i with J continues through all values of J; other diagnostics behave in a similar manner. The comparison with PIC shows the n_i transition at smaller J, corresponding to the earlier drop in T_e.

The sheath widths given in figure 7(*c*), show the usual consistency with increasing J (and n_i) in the model, until the multiplication becomes important. For the higher values of J, the sheath width drops to lower values, as also seen in the more usual α to γ transition. There are also differences between the s_{CL} values for the uniform and triangular ion source profiles in the sheaths, which can be qualitatively understood from (23), which shows $s_{CL} \propto K_{CL}/\Gamma_w$. There is a larger Γ_w in the uniform source case as seen in figure 7(*d*), but also a larger K_{CL}. We have also plotted the considerably smaller homogeneous maximum sheath width s_m (crosses). Before discussing figure 7(*d*), we comment on interesting comparisons with PIC values. At the lowest $J = 400\ A\,m^{-2}$, the PIC average T_e and sheath width s_m values are close to the triangular source model values as seen in figures 7(*a*) and (*c*). However, for increasing J, the PIC s_m falls (as does the PIC T_e) and crosses the uniform source model curve at about $J = 950\ A\,m^{-2}$. This is consistent with our PIC results, where we observed that the source, primarily Penning ionization, moves from peaking near the plasma–sheath boundary to peaking in the center of the sheaths and adopting a more uniform sheath profile as J increases from low to intermediate values. This trend can also be observed in figure 2 when comparing the He^* profiles at $J = 400$ and $2000\ A\,m^{-2}$. At the highest J values in figure 7(*c*), the PIC values start to move back toward the triangular source model. This is also consistent with our PIC results, where we observed the peak of the Penning ionization rate profiles to shift again toward the plasma–sheath boundary at the highest J values. Thus, we conclude that if we take the change in source profile into account, the model reasonably follows the PIC results.

The results for the model wall flux in figure 7(*d*) show the general proportionality $\Gamma_w \propto J^{11/6}$ at low J as expected from (5) with $\Gamma_w \propto E_w n_i$. Within the homogeneous model $E_w \propto J^{5/6}$ and $n_i \propto J$. There are, of course, deviations when multiplication becomes important. The PIC values of Γ_w show the same trends as the sheath width; i.e. that the PIC values are initially closer to the triangular source at low values of J, approach more closely to the uniform source at intermediate values of J, and then correspond more closely to the triangular source again at the highest values of J.

In figure 7(*e*), the average metastable densities n_m are given. The positive ion balance (3) shows that $n_m \propto \Gamma_w$, and since $\Gamma_w \propto J^{11/6}$, n_m also scales as $J^{11/6}$. This near quadratic scaling is verified for the values of J for which the multiplication is small ($M_P \approx 1$, $M_\gamma \approx 1$). The effects of the multiplication modify the scaling, both directly as seen in (3), and also indirectly through the more rapid increase in Γ_w within the transition.

The power absorbed by electrons per unit area scales as $S_e \propto n_e T_e$ from (A10). Using (22) to substitute for n_e gives $S_e \propto J T_e^{1/2}$. Then S_e increases linearly with J for constant T_e at low J, where multiplication is negligible as seen in figure 7(*f*). At higher J, multiplication occurs and the bulk warm temperature T_e collapses, resulting in the flattening of the S_e curve. Compared with the model, the flattening of the S_e curve occurs at lower J in PIC because T_e collapses at a lower J.

At 27.12 MHz, we did simulations at 0.3% N_2 and found that the metastable density is about 1/3 that of the 0.1% N_2 case, in agreement with the ion balance equation (14). All other PIC equilibrium parameters are roughly the same. Additionally, simulations done for the base case but with ion-impact secondary electron coefficient $\gamma = 0$, showed minimal differences at low currents, as expected. The α to γ transition occurs at slightly higher currents, as expected. At high currents, there are some differences. At $3000\ A\,m^{-2}$, $e\Gamma_w = 320\ A\,m^{-2}$ at $\gamma = 0$, compared with $400\ A\,m^{-2}$ at $\gamma = 0.25$. This leads to a larger sheath width at $\gamma = 0$ in agreement with (23). The larger sheath width also results in a larger V_{dc}.

Finally, we emphasize that most of the results shown for the model are consequences of the homogeneous solution. The wall flux Γ_w, used in the model, is taken from the subsidiary CL calculation (appendix B) using a value of $n_{is} = n_i$, where n_i is the homogeneous model ion density. The PIC n_{is} is about 0.8 of the average PIC ion density, which is one source of discrepancy between PIC and model results. The values of s_{CL}, found in figure 7(*c*) from the CL calculation, do not appear in the homogeneous model calculation. The separate value of the maximum homogeneous sheath width s_m used in the model is significantly smaller than s_{CL}, as seen in figures 7(*c*) and 8(*c*).

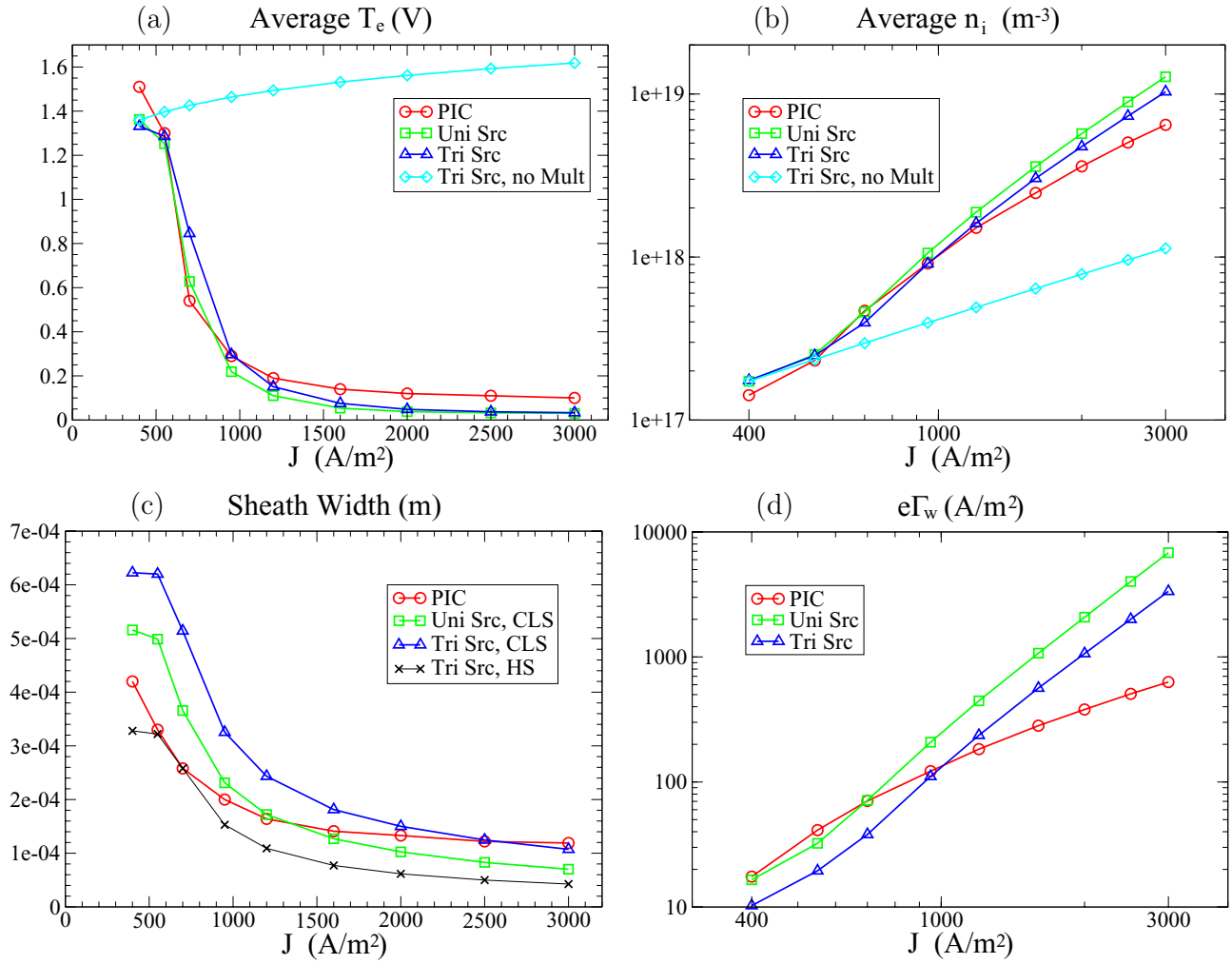

Figure 8. Comparison of the results at 13.56 MHz for PIC (circles) and theory with a uniform (squares) or triangular (triangles) ion source for $J = 400$–$3000\ \mathrm{A\,m^{-2}}$. The plots for (a)–(d) show the same diagnostics as in figure 7.

This discrepancy is also a source of the differences between the model and PIC results. The dc voltage across the sheath, V_{dc} in the CL sheath calculation (not shown), tends to follow S_e in variation. The values are $V_{dc} \approx 25$ V at $400\ \mathrm{A\,m^{-2}}$, rising linearly with J and flattening in the multiplication region to $V_{dc} \approx 150$ V (triangle source), $V_{dc} \approx 100$ V (uniform source) and $V_{dc} \approx 75$ V (PIC). As with s_{CL}, V_{dc} is not used in obtaining the homogeneous model solutions.

4.2. Variations with rf frequency

We contrast the results above, for 27.12 MHz, with the 13.56 MHz case, in figure 8, for the first four panels. For the average T_e in figure 8(a), we find a rapid fall of T_e with increasing J, for both the model and the PIC. In contrast to the higher frequency, this implies a more rapid onset of multiplication which collapses the warm temperature. Without multiplication T_e remains fairly constant, as shown. The α to γ transition in J due to the multiplication scales as ω, in agreement with the theoretical result (19). From the PIC data, taking as a transition condition that T_e drops by a factor of 2 from its low-current value, we find from (19) that the values of J at the transition for each frequency correspond to $E_{peak,T} \approx 2.3 \times 10^6\ \mathrm{V\,m^{-1}}$. This confirms our understanding that the multiplication, and therefore the transition, depends primarily on E_{peak}. The condition that T_e drops by a factor of 2 is equivalent to the bracketed term in (17) becoming very small. Thus, it corresponds to the usual transition from the α to the γ mode.

Before the collapse, at the lowest current $400\ \mathrm{A\,m^{-2}}$, the 13.56 and 27.12 MHz T_e's are roughly the same as are the densities, confirming (22) that the electron power is independent of frequency. The collapse of T_e at small J for 13.56 MHz is reflected in the average n_i, shown in figure 8(b), which increases, even at relatively small J, faster than linearly. When multiplication is suppressed in the model, the simple linear scaling is found. The flux is also larger at 13.56 MHz since from (B15) $\Gamma_w \propto (J/\omega)^{5/6} n_{is}{}^{13/12}$. The larger Γ_w is confirmed in figure 8(d). As a consequence, the metastable density is also larger, since from (3) the Penning ionization must balance the larger wall losses.

To quantitatively examine the frequency effects, we plot in figures 9 and 10 the results versus frequency at a low current of $400\ \mathrm{A\,m^{-2}}$ and a high current of $3000\ \mathrm{A\,m^{-2}}$, respectively. The four frequencies investigated are 13.56, 20.34, 27.12 and 40.68 MHz. At low current, figure 9(a) shows that T_e remains

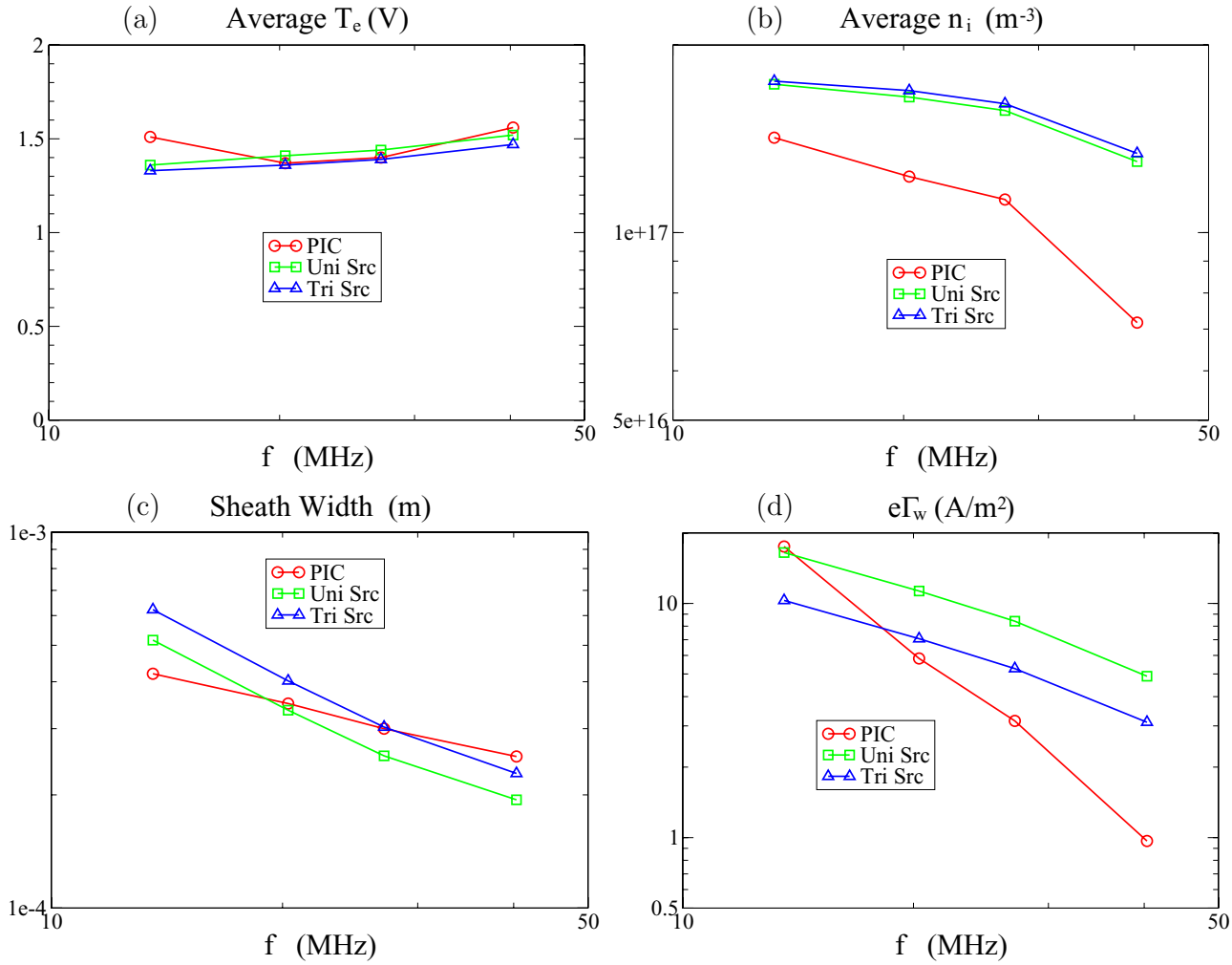

Figure 9. Comparison of the results at $J = 400\,\mathrm{A\,m^{-2}}$ for PIC (circles) and theory with a uniform (squares) or triangular (triangles) ion source for $f = 13.56$–$40.68\,\mathrm{MHz}$, showing: (*a*) average T_e (V), (*b*) average n_i ($\mathrm{m^{-3}}$), (*c*) sheath width (m) and (*d*) ion wall current $e\Gamma_w$ ($\mathrm{A\,m^{-2}}$).

high and nearly constant over the entire range, indicating that multiplication is small and that the discharge remains in the α-mode. In contrast, at high current, figure 10(*a*) shows that T_e increases with frequency, indicating a transition from γ mode at 13.56 MHz to α mode at 40.68 MHz. This is not surprising and confirms the scaling in (19) that $J \propto \omega$ for the α to γ transition. Such a transition has also been seen both in simulations [29] and in experiments [3] for a pure helium feed gas. Figure 9(*b*) indicates that the electron density decreases weakly with frequency. This can be understood from the electron power balance (21), since at the small J and with $T_e \approx$ const, the second term gives the decrease in density with frequency seen in both the PIC data and the model. The model density is higher than the PIC density because the model density is uniform, i.e. does not account for the drop in density within the CL sheaths, as seen in the PIC data. At the higher current, the second term in (21) becomes negligible, and we see in figure 9(*b*) the scaling $n_e \propto 1/\sqrt{T_e}$ as in (22).

At low current both the sheath width and the ion flux decrease with increasing frequency, as seen in figures 9(*c*) and (*d*). From (B15), we expect that $\Gamma_w \propto (J/\omega)^{5/6} {n_{is}}^{13/12}$, which is roughly seen in figure 9(*d*). The sheath width scaling (23) is also roughly seen. However, the PIC data show a shift from a uniform ion source profile at 13.56 MHz to a more triangular source at the two intermediate frequencies; then, to a source mainly within the bulk plasma at the highest frequency of 40.68 MHz. In contrast, at the higher current, the sheath width in figure 10(*c*) increases with frequency, while Γ_w in figure 10(*d*) decreases. These data reflect the transition from the γ to the α mode with increasing frequency. Because n_i falls rapidly during this transition, the flux Γ_w falls correspondingly, although the effect is seen more in the model than in the PIC. The sheath width $s_{CL} \propto \Gamma_w^{-1}$, so the sheath width increases.

To examine these shifts, we plot in figure 11 the CL sheath coefficient K_{CL} from (23) versus f, using the PIC data given in figures 9(*c*) and (*d*). As expected, at a low current of $400\,\mathrm{A\,m^{-2}}$, K_{CL} falls continuously as f increases (circles). At a higher current of $3000\,\mathrm{A\,m^{-2}}$ (squares), the PIC data show an ion source profile shift *opposite* to the low-current case; i.e. the source is mainly within the bulk plasma at low frequency, and shifts toward a uniform profile in the sheath at the highest frequency.

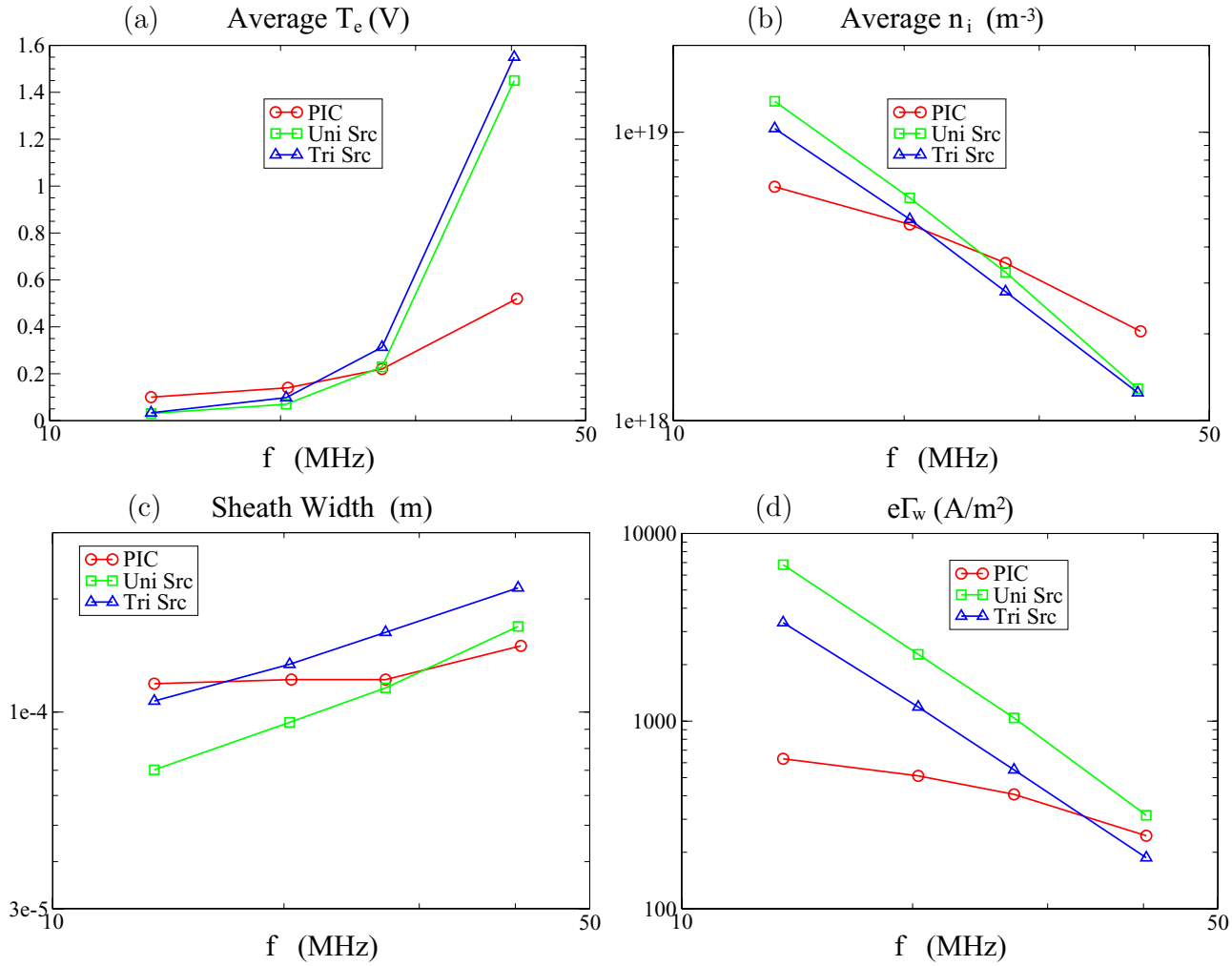

Figure 10. Comparison of the results at $J = 3000\,\mathrm{A\,m^{-2}}$ for PIC (circles) and theory with a uniform (squares) or triangular (triangles) ion source for $f = 13.56$–$40.68\,\mathrm{MHz}$. The plots for (a)–(d) show the same diagnostics as in figure 9.

5. Conclusions and further discussion

We previously developed a global model to study atmospheric pressure capacitive discharges using a helium gas feed with a small admixture of a reactive gas. However, the model neglected high-power effects such as electron multiplication in the sheaths. In this paper, we improve the model to include these effects and then compare the model to 1D PIC simulations. The new model has two electron classes: higher temperature 'hot' electrons associated with the high-field sheath regions and cooler 'warm' electrons associated with the plasma bulk and the low-field sheath regions. There is also a separate Child law sheath calculation to determine the wall flux Γ_w self-consistently. We mainly studied an atmospheric pressure He/0.1%N_2 parallel-plate discharge with a 1 mm gap. When the input rf current was varied from $J = 400$ to $6000\,\mathrm{A\,m^{-2}}$, the discharge transitioned from a low-power discharge with essentially no sheath multiplication to a high-power discharge in which electron–ion pair production is dominated by sheath multiplication. As we raise the frequency from 13.56 to 40.68 MHz, this transition occurs at increasingly higher J. In addition to validating the global model results, the PIC simulations supply interesting spatial information that can be used to improve global model accuracy.

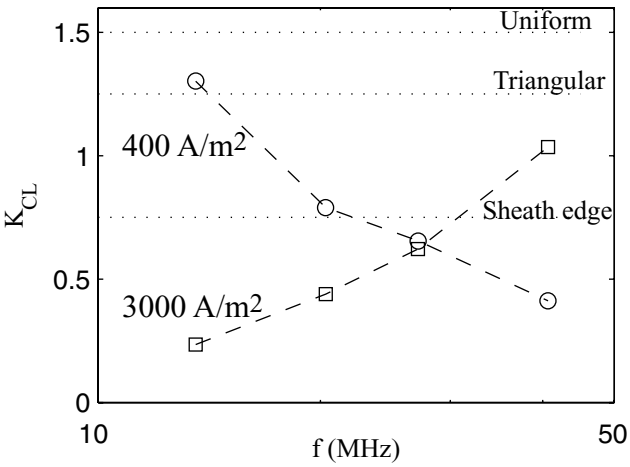

Figure 11. CL coefficient K_{CL} versus frequency f for the PIC data at $J = 400\,\mathrm{A\,m^{-2}}$ (circles) and $J = 3000\,\mathrm{A\,m^{-2}}$ (squares).

Some important conclusions that can be drawn from a combination of the PIC and global model results, as well as

their analytical scaling, are given below.

(1) A two-temperature model with hot and warm electrons and sheath multiplication can be used to explain the PIC results over a wide range of currents and frequencies. The hot-electron density n_h is always much lower than n_e, but the production of the helium metastables by the hot and warm electrons may be comparable in the α mode and is dominated by the hot electrons in the γ mode.
(2) Most of the electron–ion pair production is due to Penning ionization, which is generally over an order of magnitude greater than electron-impact ionization. About half of the Penning ionization occurs in the high-field sheath regions, and the rest in the bulk and low-field sheath regions.
(3) There is an α to γ transition with increasing rf current or decreasing rf frequency. It occurs when the electron multiplication in the high-field regions becomes equal to the Penning ionization in the bulk and low-field sheath regions. The transition condition is $2J/(\omega\epsilon_0) = E_{peak,T} \approx 2 \times 10^6\,\mathrm{V\,m^{-1}}$, where $E_{peak,T}$ is the space-and-time-maximum sheath electric field at atmospheric pressure. The signature of the transition is the collapse of T_e in the plasma bulk.
(4) As seen from (22), $n_e \propto J/{T_e}^{1/2}$. Therefore, n_e increases faster than linearly with J through the transition. At fixed J and decreasing frequency, the increase in n_e after the transition is equal to the square root of the ratio of T_e before and after the collapse of T_e in the bulk. This increase can be quite large and results in a reduction in the sheath width.
(5) A Child law sheath, with ion generation in the sheaths, gives reasonable estimates of the sheath widths and the ion losses to the walls.
(6) There are significant ion source profile effects on the transition condition and equilibrium quantities (up to a factor of two). At low currents and low frequencies, most of the metastable helium and therefore the Penning ionization is spread over the sheaths; as the frequency increases, the ionization moves toward the bulk-sheath boundary. At high currents and low frequencies, the Penning ionization peaks near the bulk-sheath boundary; as the frequency increases the ionization moves toward the central sheath regions. A triangular ion source in the sheaths is found to be a reasonable choice over the range of currents and frequencies considered.

The homogeneous model fields, sheath widths and densities cannot fully capture the corresponding PIC results. For example, at a given frequency, the α to γ transition occurs at a somewhat different current in the model and the PIC simulations, a difference that varies with frequency. The use of an additional Child law sheath calculation to determine the ion wall flux self-consistently with the homogeneous model calculation partly mitigates the discrepancies between the model and the PIC results.

Acknowledgments

This work was partially supported by the Department of Energy Office of Fusion Energy Science Contract DE-SC000193 and the University of California France-Berkeley Fund.

Appendix A. Summary of single temperature model

A single electron temperature, homogeneous discharge model was used previously to describe the dynamics of a high-pressure discharge on the rf timescale [25, 30, 31]. By high pressure we mean $\nu \gg \omega$, where ν is the electron–neutral momentum transfer frequency and ω is the radian rf frequency. A sinusoidal rf current density $J_{rf}(t) = \mathrm{Re}\left(J\,\mathrm{e}^{\mathrm{j}\omega t}\right)$, with J the complex amplitude (a complex number), flows through the discharge gap from $x = 0$ to $x = l$. The net heavy-particle positive charge density is assumed to be uniform and constant, $\rho_0 = en_i$, everywhere within the gap. An electron cloud of uniform density n_e and fixed width $d < l$ oscillates within the gap in response to the rf excitation, leading to the appearance of oscillating rf sheath regions near each electrode. The complex amplitude of the current density flowing in the bulk plasma (oscillating electron cloud) is the sum of conduction and displacement components, $J = J_c + J_d$, where $J_c = (\kappa - 1)J/\kappa$ and $J_d = J/\kappa = \mathrm{j}\omega\epsilon_0 E_b$. Here ϵ_0 is the free space permittivity, E_b is the bulk electric field complex amplitude, and

$$\kappa = 1 - \frac{\omega_p^2}{\omega(\omega - j\nu)} \equiv \kappa_R + \mathrm{j}\kappa_I \tag{A1}$$

is the complex plasma dielectric constant, having real and imaginary parts $\kappa_R = 1 - \omega_p^2/\nu^2 \approx 1$ and $\kappa_I = -\omega_p^2/\omega\nu$, with $\omega_p = (e^2 n_e/\epsilon_0 m_e)^{1/2}$ the electron plasma frequency. The electron sheath width near each electrode oscillates from $x = 0$ to $x = 2\bar{s}$, where s is the complex amplitude and $\bar{s} = |s|$. The two sheaths oscillate 180° out-of-phase, leading to a rigid oscillation of the electron cloud, with a bulk width $d = l - 2\bar{s}$. The sheath oscillation $s(t)$ and the sheath electric field $E(x, t)$ are [18]

$$s(t) = \frac{1}{2}s_m(1 - \cos\omega t), \tag{A2}$$

$$E(x,t) = \frac{en_e s_m}{2\epsilon_0}\left(\frac{2x}{s_m} - 1 + \cos\omega t + \frac{\omega\nu}{\omega_p^2}\sin\omega t\right). \tag{A3}$$

This leads to a time-varying ohmic electron power density

$$P_c(t) = \overline{P}_c[1 + \cos(2\omega t - \theta)], \tag{A4}$$

where θ is the phase angle between J_c and E_b, and

$$\overline{P}_c = \frac{1}{2}\mathrm{Re}(J_c \cdot E_b^*) = -\frac{1}{2}\frac{|J|^2}{\omega\epsilon_0}\frac{\kappa_I}{\kappa_R^2 + \kappa_I^2}. \tag{A5}$$

The sheath oscillation complex amplitude is found to be

$$s = \frac{|J|\,\mathrm{e}^{-\mathrm{j}\theta}}{en_e\omega}\left(\frac{(1-\kappa_R)^2 + \kappa_I^2}{\kappa_R^2 + \kappa_I^2}\right)^{1/2}. \tag{A6}$$

The electron temperature T_e is assumed to be uniform in the bulk plasma and oscillates sinusoidally in time [32, section 6.3]. The ion density and by quasineutrality, the electron density n_e are uniform and independent of time. Then the electron energy balance is

$$\frac{\mathrm{d}T_e}{\mathrm{d}t} = \frac{2}{3}\frac{P_c(t)}{en_e} - \frac{2}{3}\nu\frac{3m_e}{m_{He}}T_e - \sum_j \frac{2}{3}\nu_j\mathcal{E}_j, \tag{A7}$$

where T_e is the electron temperature in volts, ν is the electron–neutral elastic collision frequency, m_e and m_{He} are the electron and neutral helium masses, ν_j are the inelastic collision frequencies, $\mathcal{E}_j$ are the inelastic energy losses in volts per collision, and $P_c(t)$ is given by (A4). To incorporate the inelastic energy losses into the model, a correction factor ζ to ν is introduced, $\bar{\nu}_\epsilon = \overline{\zeta(2m_e/m_{He})}\nu$ with

$$\zeta = 1 + \sum_j \frac{m_{He}}{3m_e}\frac{\nu_j \mathcal{E}_j}{\nu T_e}. \tag{A8}$$

The solution for T_e was obtained as

$$T_e(t) = T_{e0} + T_{e1}\cos(2\omega t - \phi_0), \tag{A9}$$

where $T_{e0} = P_{c0}/\bar{\nu}_\epsilon$, $T_{e1} = P_{c0}/(4\omega^2 + \bar{\nu}_\epsilon^2)^{1/2}$, $P_{c0} = 2\overline{P}_c/3en_e$, and $\phi_0 = \theta + \arctan(2\omega/\bar{\nu}_\epsilon)$. The temperature oscillates between the minimum value $T_{emin} = T_{e0} - T_{e1}$ and the maximum value $T_{emax} = T_{e0} + T_{e1}$ at twice the rf frequency. The time-average energy balance is

$$-\frac{1}{2}\frac{|J|^2}{\omega\epsilon_0}\frac{\kappa_I}{\kappa_R^2 + \kappa_I^2} = \frac{3}{2}en_e\bar{\nu}_\epsilon T_{e0}. \tag{A10}$$

The rate coefficients for electron-activated processes with high activation energies $\mathcal{E}_a$ are strongly affected by the oscillating electron temperature. Expressing the Maxwellian rate coefficients in the form $K = K_0\exp(-\mathcal{E}_a/T_e)$, where the pre-exponential factor K_0 is a weak function of T_e, then the mean rate coefficient was determined by averaging over the oscillating temperature, with K_0 set to its maximum value, to be

$$\overline{K} = K_0(T_{emax})\,\mathrm{erfc}\left(\sqrt{\mathcal{E}_a/T_{emax}}\right), \tag{A11}$$

where erfc is the complementary error function.

Appendix B. Self-consistent rf sheath

The Child–Langmuir sheath width s_{CL} and wall flux Γ_w are found from the self-consistent collisional CL rf sheath model in [33], but with a constant mobility and the addition of a triangular ion source profile in the sheath. The sheath motion $x(\phi)$ ($\phi \equiv \omega t$) is given by

$$-en_i\omega\frac{dx}{d\phi} = -J\sin\phi, \tag{B1}$$

where $n_i(x)$ is the ion density, $J = en_{is}\omega s_0$ is the rf current amplitude and s_0 is the sheath oscillation amplitude in the plasma near the sheath edge. The oscillation extends from the plasma–sheath edge designated as $x = 0$ to the wall at $x = s_{CL}$. For a triangular profile, the ion source within the sheath is $G(x) = 2\Gamma_w(s_{CL} - x)/s_{CL}^2$, and the resulting ion flux $\Gamma(x) = \int_0^x G(x')\,dx'$ is

$$\Gamma(x) = \Gamma_w\frac{2s_{CL}x - x^2}{s_{CL}^2}. \tag{B2}$$

This can be equated to the mobility-driven flux

$$\Gamma_w\frac{2s_{CL}x - x^2}{s_{CL}^2} = \mu_i n_i\overline{E}, \tag{B3}$$

where the dc electric field in the sheath is [33, equation (10)]

$$\overline{E} = \frac{J}{\pi\omega\epsilon_0}(\sin\phi - \phi\cos\phi). \tag{B4}$$

Solving (B3) for n_i and inserting this and $\overline{E}$ from (B4) into (B1), we obtain

$$\Gamma_w\frac{2s_{CL}x - x^2}{s_{CL}^2}\,dx = \frac{\mu_i J^2}{\pi e\omega^2\epsilon_0}\sin\phi\,(\sin\phi - \phi\cos\phi)\,d\phi. \tag{B5}$$

Integrating this equation gives

$$\frac{\Gamma_w}{s_{CL}^2}\left(s_{CL}x^2 - \frac{x^3}{3}\right) = \frac{\mu_i J^2}{\pi e\omega^2\epsilon_0}\left(\frac{\phi}{2} - \frac{3}{8}\sin 2\phi + \frac{\phi}{4}\cos 2\phi\right), \tag{B6}$$

which can be solved for the sheath motion $x(\phi)$. Setting $x = s_{CL}$ at $\phi = \pi$ in (B6), we obtain the CL sheath width

$$s_{CL} = \frac{9}{8}\frac{\mu_i J^2}{e\omega^2\epsilon_0}\frac{1}{\Gamma_w}. \tag{B7}$$

Various approaches can be used to determine Γ_w as a function of the plasma density n_{is} where the plasma and sheath join [22, 34]. We use a simple analytical approach based on the collisional Bohm speed $u_B = \mu_i E_s$, where

$$E_s = \frac{T_e}{N\lambda_{Ds}} = \frac{T_e}{N}\left(\frac{en_{is}}{\epsilon_0 T_e}\right)^{1/2}, \tag{B8}$$

with λ_{Ds} the electron Debye length at the joining position. Godyak and Sternberg [22] give $N = 1$ as the joining condition, but for $N = 1$, the charge density ρ is equal to en_i for the ambipolar diffusion solution in the bulk plasma, and thus cannot be joined to the rf sheath solution near $x = 0$. The PIC simulation results for E_s indicate a joining condition for $N \approx 5$, corresponding to $\rho \approx 0.04\,en_i$. However, as shown below, the overall equilibrium is insensitive to the exact choice of N. Using $n_{is} = \Gamma_{is}/\mu_i E_s$, with Γ_{is} from (B2) in (B8), we obtain

$$E_s^3(\phi_s) = \frac{eT_e}{\mu_i N^2\epsilon_0}\cdot\Gamma_w\frac{2s_{CL}x - x^2}{s_{CL}^2}, \tag{B9}$$

which determines the joining phase ϕ_s. Since the join occurs for $x_s \ll s_{CL}$ (typically $x_s/s_{CL} \sim 0.03$–0.1 for the parameters of the PIC simulations), we expand the left- and right-hand sides of (B9) in power series and keep only the first non-zero terms to obtain

$$\left(\frac{J}{\pi\omega\epsilon_0}\right)^3\frac{\phi_s^9}{27} = \frac{2eT_e\Gamma_w}{\mu_i N^2\epsilon_0}\left(\frac{8}{9\pi}\right)^{1/2}\frac{\phi_s^{5/2}}{\sqrt{15}}. \tag{B10}$$

Solving for the joining phase ϕ_s, we obtain

$$\phi_s = \left[\left(\frac{32}{135\pi}\right)^{1/2}\left(\frac{3\pi\omega\epsilon_0}{J}\right)^3\frac{eT_e}{\mu_i N^2\epsilon_0}\Gamma_w\right]^{2/13}. \tag{B11}$$

The density n_{is} at the joining phase is found from (B8) to be

$$n_{is} = \frac{N^2\epsilon_0}{eT_e}E_s^2. \tag{B12}$$

Using the power series expansion

$$E_s^2 = \left(\frac{J}{\pi\omega\epsilon}\right)^2\frac{\phi_s^6}{9}, \tag{B13}$$

we obtain

$$n_{is} = 3^{4/13}\left(\frac{32}{45\pi}\right)^{6/13}\left(\frac{N^2\epsilon_0}{eT_e}\right)^{1/13}\left(\frac{\pi\omega\epsilon_0}{J}\right)^{10/13}\left(\frac{\Gamma_w}{\mu_i}\right)^{12/13}. \tag{B14}$$

Solving (B14) for Γ_w as a function of n_{is} and evaluating the numerical coefficients gives

$$\Gamma_w = 0.56\,\mu_i\left(\frac{eT_e}{N^2\epsilon_0}\right)^{1/12}\left(\frac{J}{\omega\epsilon_0}\right)^{5/6}n_{is}{}^{13/12}, \tag{B15}$$

which gives a slightly nonlinear dependence of Γ_w on n_{is}, with a weak dependence on N. Γ_w can also be written simply using (B8), with $N = 5$, as

$$\Gamma_w = 0.56\,\mu_i E_s^{1/6}E_w^{5/6}n_{is}, \tag{B16}$$

where E_s given by (B8) and $E_w = J/\omega\epsilon_0$ are the dc electric fields at the joining position and at the wall, respectively. Evaluating the wall density $n_{iw} = \Gamma_w/\mu_i E_w$, we obtain the density ratio $n_{iw}/n_{is} = 0.56(E_s/E_w)^{1/6}$. Finally, the dc voltage across the sheath can be evaluated from

$$V = \int_0^\pi \mathrm{d}\phi\, E(\phi)\frac{\mathrm{d}x}{\mathrm{d}\phi}, \tag{B17}$$

yielding $V = 0.48\,E_w s_{CL}$. (A similar calculation done for a *uniform* ion source profile in the sheath gives the same scalings with different coefficients: $9/8 \to 3/2$ in the CL sheath width, $0.56 \to 0.92$ for the ion flux, and $0.48 \to 0.44$ for the dc voltage.)

The ion power per unit volume for the constant mobility sheath is $p_i(x,\omega t) = e\mu_i n_i(x)E(x,\omega t)\cdot E(x,\omega t)$, with

$$E = \frac{J}{\omega\epsilon_0}\big(\cos\omega t - \cos\phi(x)\big), \qquad \omega t < \phi(x), \tag{B18}$$
$$= 0, \qquad \text{otherwise},$$

the time- and space-varying electric field in the sheath [33]. Integrating p_i over the sheath, we obtain

$$S_i = e\mu_i\left(\frac{J}{\omega\epsilon_0}\right)^2\cdot\frac{1}{\pi}\int_0^\pi \mathrm{d}(\omega t) \times\int_{s(\omega t)}^{s_{CL}}\mathrm{d}x\, n_i\,(\cos\omega t - \cos\phi)^2\,. \tag{B19}$$

Using (B1) to transform the inner integral from x to ϕ, we obtain

$$S_i = \frac{\mu_i J^3}{\omega^3\epsilon_0^2}\cdot\frac{1}{\pi}\int_0^\pi \mathrm{d}(\omega t)\int_{\omega t}^\pi \mathrm{d}\phi\,\sin\phi\,(\cos\omega t - \cos\phi)^2\,. \tag{B20}$$

The double integral yields $5\pi/6$. Hence we obtain (for a single sheath) the ion power per unit area

$$S_i = \frac{5\mu_i J^3}{6\omega^3\epsilon_0^2}, \tag{B21}$$

which is used in the model.

References

[1] Knake N, Reuter S, Niemi K, Schulz-von der Gathen V and Winter J 2008 *J. Phys. D: Appl. Phys.* **41** 194006
[2] Schulz-von der Gathen V, Schaper L, Knake N, Reuter S, Niemi K, Gans T and Winter J 2008 *J. Phys. D: Appl. Phys.* **41** 194004
[3] Liu D W, Iza F and Kong M G 2009 *Plasma Process. Polym.* **6** 446
[4] Ellerweg D, Benedikt J, von Keudell A, Knake N and Schulz-von der Gathen V 2010 *New J. Phys.* **12** 013021
[5] Bibinov N, Knake N, Bahre H, Awakowicz P and Schulz-von der Gathen V 2011 *J. Phys. D: Appl. Phys.* **44** 345204
[6] Park G, Lee H, Kim G and Lee J K 2008 *Plasma Process. Polym.* **5** 569
[7] Park G, Hong Y, Lee H, Sim J and Lee J K 2010 *Plasma Process. Polym.* **7** 281
[8] Liu D X, Rong M Z, Wang X H, Iza F, Kong M G and Bruggeman P 2010 *Plasma Process. Polym.* **7** 846
[9] Stafford D S and Kushner M J 2004 *J. Appl. Phys.* **96** 2451
[10] Iza F, Lee J K and Kong M G 2007 *Phys. Rev. Lett.* **99** 075004
[11] Liu D W, Iza F and Kong M G 2008 *Appl. Phys. Lett.* **93** 261503
[12] Martens T, Bogaerts A, Brok W J M and Dijk P V 2008 *Appl. Phys. Lett.* **92** 041504
[13] Hong Y J, Moon M, Iza F, Kim G C and Lee J K 2008 *J. Phys. D: Appl. Phys.* **41** 245208
[14] Waskoenig J 2010 *PhD Thesis* Queen's University Belfast
[15] Waskoenig J, Niemi K, Knake N, Graham L M, Reuter S, Schulz-von der Gathen V and Gans T 2010 *Plasma Sources Sci. Technol.* **19** 045018
[16] Hemke T, Eremin D, Mussenbrock T, Derzsi A, Donko Z, Dittmann K, Meichsner J and Schulze J 2013 *Plasma Sources Sci. Technol.* **22** 015012
[17] Lee H W, Park G Y, Seo Y S, Im Y H, Shin S B and Lee H J 2011 *J. Phys. D: Appl. Phys.* **44** 053001
[18] Lazzaroni C, Chabert P, Lieberman M A, Lichtenberg A J and Leblanc A 2012 *Plasma Sources Sci. Technol.* **21** 035013
[19] Verboncoeur J P, Alves M V, Vahedi V and Birdsall C K 1993 *J. Comput. Phys.* **104** 321
[20] Vahedi V and Surendra M 1995 *Comput. Phys. Commun.* **87** 179
[21] Morgan W L 2012 *The Morgan Database, Kinema Research and Software* www.lxcat.laplace.univ-tlse.fr, retrieved on April 12
[22] Godyak V A and Sternberg N 1990 *IEEE Trans. Plasma Sci.* **18** 159
[23] Hagelaar G J M and Pitchford L C 2005 *Plasma Sources Sci. Technol.* **14** 722
[24] Lazzaroni C, Lieberman M A, Lichtenberg A J and Chabert P 2012 *J. Phys. D: Appl. Phys.* **45** 495204
[25] Godyak V A and Khanneh A S 1986 *IEEE Trans. Plasma Sci.* **14** 112
[26] Raizer Y P 1991 *Gas discharge physics* (Berlin: Springer)
[27] Niemi K, O'Connell D, de Oliverira N, Joyeaux D, Nahon L, Booth J and Gans T 2013 *Appl. Phys. Lett.* **103** 034102
[28] Wagenaars E, Gans T, O'Connell D and Niemi K 2012 *Plasma Sources Sci. Technol.* **21** 042002
[29] Shi J J and Kong M G 2005 *Appl. Phys. Lett.* **87** 201501
[30] Lieberman M A and Lichtenberg A J 2005 *Principles of Plasma Discharges and Materials Processing* 2nd edn (New York: Wiley-Interscience)
[31] Chabert P and Braithwaite N 2011 *Physics of Radiofrequency Plasmas* (Cambridge: Cambridge University Press)
[32] Makabe T and Petrovic Z L 2006 *Plasma Electronics: Applications in Microelectronic Device Fabrication* (London: Taylor and Francis)
[33] Lieberman M A 1989 *IEEE Trans. Plasma Sci.* **17** 338
[34] Brinkmann R 2009 *J. Phys. D: Appl. Phys.* **42** 194009